PAPER

# Overfitting Problem of ANN- and VSTF-Based Nonlinear Equalizers Trained on Repeated Random Bit Sequences

**Kai IKUTA**[†a)], ***Student Member***, **Jinya NAKAMURA**[††], ***Nonmember***, *and* **Moriya NAKAMURA**[†], ***Member***

**SUMMARY** In this paper, we investigated the overfitting characteristics of nonlinear equalizers based on an artificial neural network (ANN) and the Volterra series transfer function (VSTF), which were designed to compensate for optical nonlinear waveform distortion in optical fiber communication systems. Linear waveform distortion caused by, e.g., chromatic dispersion (CD) is commonly compensated by linear equalizers using digital signal processing (DSP) in digital coherent receivers. However, mitigation of nonlinear waveform distortion is considered to be one of the next important issues. An ANN-based nonlinear equalizer is one possible candidate for solving this problem. However, the risk of overfitting of ANNs is one obstacle in using the technology in practical applications. We evaluated and compared the overfitting of ANN- and conventional VSTF-based nonlinear equalizers used to compensate for optical nonlinear distortion. The equalizers were trained on repeated random bit sequences (RRBSs), while varying the length of the bit sequences. When the number of hidden-layer units of the ANN was as large as 100 or 1000, the overfitting characteristics were comparable to those of the VSTF. However, when the number of hidden-layer units was 10, which is usually enough to compensate for optical nonlinear distortion, the overfitting was weaker than that of the VSTF. Furthermore, we confirmed that even commonly used finite impulse response (FIR) filters showed overfitting to the RRBS when the length of the RRBS was equal to or shorter than the length of the tapped delay line of the filters. Conversely, when the RRBS used for the training was sufficiently longer than the tapped delay line, the overfitting could be suppressed, even when using an ANN-based nonlinear equalizer with 10 hidden-layer units.
***key words:*** *optical nonlinear compensation, nonlinear equalizers, artificial neural network, Volterra series transfer function, overfitting*

## 1. Introduction

Data traffic through communication systems has been continuing to grow exponentially with the technological development of cloud computing and fifth-generation (5G) mobile communications. Increasing the capacity further will require optical fiber communications technology that supports these services. To meet this demand, multi-level modulation, including quadrature amplitude modulation (QAM), is an important technology that can increase the spectral efficiency in the limited optical bandwidth. However, a QAM signal has a large peak-to-average power ratio (PAPR) and is susceptible to nonlinear waveform distortion caused by optical nonlinear effects such as self-phase modulation (SPM) and cross-phase modulation (XPM). Techniques to compensate for the nonlinear waveform distortion using digital signal processing (DSP), digital backpropagation (DBP) and nonlinear equalizers based on the Volterra series transfer function (VSTF) have been studied [1]–[4]. However, the significant computational complexity of these methods poses a technical barrier to their practical implementation. On the other hand, nonlinear equalizers based on artificial neural networks (ANNs) are attracting attention as another possible candidate. ANN-based nonlinear equalizers have been experimentally demonstrated with various modulation formats, including intensity modulation and direct detection (IM/DD), QAM, and orthogonal frequency-division multiplexing (OFDM) [5]–[7]. The effectiveness of the equalizers has been verified not only in laboratory experiments but also with an 11,000-km live-traffic carrying submarine cable [8]. Recently, several field-programmable gate array (FPGA) implementations of ANN-based nonlinear equalizers have been demonstrated [9], [10]. One implementation realized both the equalization and training stages within the same FPGA simultaneously [11]. In our research group, we demonstrated complex-valued ANN-based nonlinear equalizers, which showed improved learning speed and reduced computational complexity compared to a conventional real-valued ANN [12]. Furthermore, we clarified the necessary number of ANN units for compensating for chromatic dispersion (CD) and SPM [13]. We also reported that an ANN can effectively compensate for nonlinearities using significantly less computational effort compared to DBP and the VSTF [14], [15].

An issue that has been pointed out with the ANN-based nonlinear equalizers is overfitting. In particular, when a pseudo-random binary sequence (PRBS) is used in the training, the ANN configures a logic circuit that is optimized for the specific PRBS [16]–[18]. Consequently, the ANN predicts the incoming PRBS signals, resulting in overestimation of the compensation performance. Conversely, when the compensation performance is evaluated using a PRBS different from the one used in the training, the compensation performance is underestimated. Some reports investigated the dependence of the tap length of the ANN and the length of the PRBS on the overfitting characteristics [19], [20]. It is also reported that the overfitting becomes stronger when the number of hidden-layer of the ANN is increased from three to four [21]. We evaluated the overfitting characteristics of VSTF-based nonlinear equalizers using the same method that has been employed to evaluate the overfitting of ANN-based nonlinear equalizers. As a result, we revealed that the overfitting of the ANN- and VSTF-based nonlinear

Manuscript received July 17, 2023.
Manuscript revised September 29, 2023.
Manuscript publicized January 30, 2024.
[†]The authors are with Meiji University, Kawasaki-shi, 214-8571 Japan.
[††]The author is with Fujikura Ltd., Tokyo, 135-8512 Japan.
a) E-mail: k_ikuta@meiji.ac.jp
DOI: 10.23919/transcom.2023EBP3121

equalizers occurs under the same conditions when PRBSs are used in the training [22]. This is because the VSTF has a high function representation capability and thus acquires the logic circuit of the PRBS as well as the ANN. We should consider that the overfitting is not a problem that is unique to ANN-based nonlinear equalizers but possibly occurs with any equalizers using learning algorithms.

In addition to PRBSs, the overfitting characteristics of the ANN-based nonlinear equalizers have also been investigated in a case where finite-length repeated random bit sequences (RRBSs) were used in the training [16]–[18]. As the number of input and hidden layer units in the ANN is increased, the ANN-based nonlinear equalizers have a higher function representation capability to memorize the random bit sequence, resulting in overfitting. However, it is known that the overfitting of ANN-based nonlinear equalizers with an RRBS is weaker than that with a PRBS. On the other hand, the overfitting characteristics of VSTF-based nonlinear equalizers with an RRBS have not been investigated, to the authors' best knowledge. Therefore, it remains unclear whether the overfitting of ANN-based nonlinear equalizers with an RRBS is larger than that of the VSTF. This paper focuses on comparing the overfitting characteristics of the ANN- and VSTF-based nonlinear equalizers trained on RRBSs, in contrast to the characteristics of the ANN trained on PRBS, which were investigated in [19], [20].

In this study, we evaluated and compared the overfitting characteristics of nonlinear equalizers based on the ANN and VSTF which were trained on a finite-length RRBS. We clarified that the overfitting characteristics of the ANN-based nonlinear equalizer were comparable to those of the VSTF when the number of hidden-layer units of the ANN was as large as 100 or 1000. However, when the number of hidden-layer units was 10, which is usually enough to compensate for optical nonlinear distortion, the overfitting was weaker than that of the VSTF.

The remainder of this paper is organized as follows: Section 2 summarizes the theory and computational complexity of ANN- and VSTF-based nonlinear equalizers. In Sect. 3, we explain the system setup for evaluating overfitting characteristics. Section 4 offers a comparison between the overfitting of the ANN and that of the VSTF. Finally, Sect. 5 provides the conclusion of this paper.

## 2. ANN- and VSTF-Based Nonlinear Equalizers and Computational Complexity

### 2.1 ANN-Based Nonlinear Equalizer

Figure 1(a) shows the construction of the ANN-based nonlinear equalizer used for optical nonlinear compensation [12]. The ANN consists of three layers: an input layer, a hidden layer, and an output layer. Input signal $x(n)$ is fed to the input layer through a feedforward tapped delay line, where $n$ represents the time index of the sampled signal with a sampling interval of $T$. $L = 2N + 1$ expresses the tap length of the tapped delay line. $y(n)$ is the output signal of the ANN-

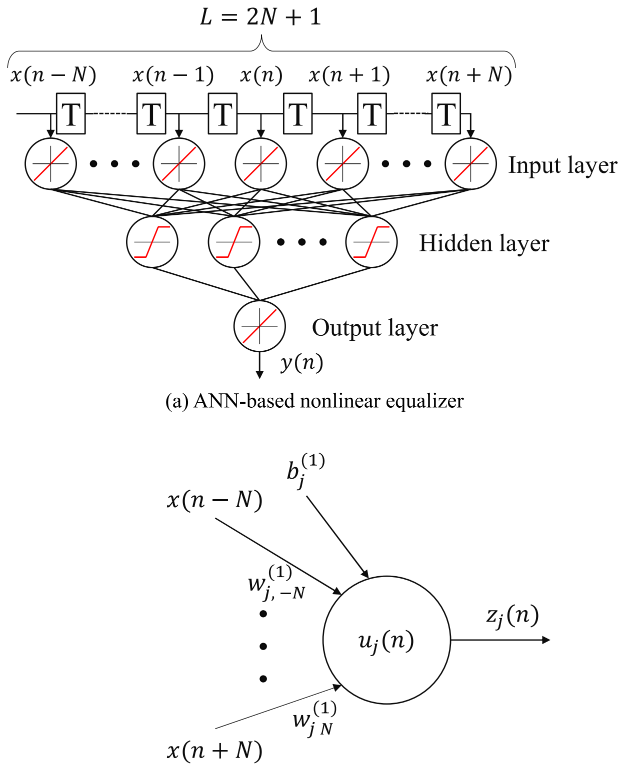


(a) ANN-based nonlinear equalizer

(b) Hidden-layer unit

**Fig. 1** ANN-based nonlinear equalizer and hidden-layer.

based nonlinear equalizer. $x(n)$ and $y(n)$ are real values, while complex values are employed in [12]. This is because binary signals are used in this investigation of the overfitting. Therefore, we employed a real-valued ANN. Input-layer units simply distribute the input signal to the hidden-layer units. Figure 1(b) shows a hidden-layer unit used in the ANN. The inner potential of the $j$-th hidden-layer unit, $u_j(n)$, is described as

$$u_j(n) = \sum_{i=-N}^{N} w_{ji}^{(1)} x(n+i) + b_j^{(1)}, \tag{1}$$

where $w_{ji}^{(1)}$ is the weight between the $i$-th input-layer unit and the $j$-th hidden-layer unit, and $b_j^{(1)}$ is the bias. The units in the hidden layer have a sigmoid function expressed as

$$z_j(n) = \frac{1}{1 + e^{-u_j(n)}}, \tag{2}$$

where $z_j(n)$ is the output of the hidden-layer unit. The units in the output layer have a linear function. The output of the ANN-based nonlinear equalizer, $y(n)$, is described as unit.

$$y(n) = \sum_{j=1}^{M} w_j^{(2)} z_j(n) + b^{(2)}, \tag{3}$$

where $w_j^{(2)}$ is the weight between the $j$-th hidden-layer unit and the output-layer unit, and $b^{(2)}$ is the bias. $M$ is the number

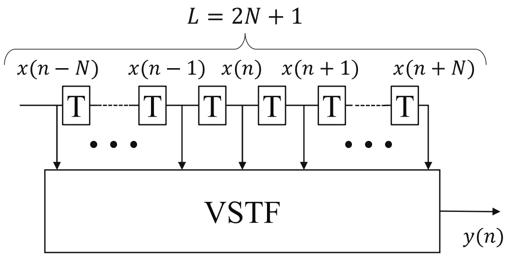


**Fig. 2** VSTF-based nonlinear equalizer.

of hidden-layer units. We trained the ANN by using the error backpropagation (EBP) method, a type of least mean square (LMS) algorithm. We trained the ANN sample by sample. We did not use batches or minibatches. The error function is described as

$$e(n) = |y(n) - t(n)|^2, \tag{4}$$

where $t(n)$ is the ideal signal point at the time index $n$, namely a *supervised signal*. The error, $e(n)$, is minimized by updating the weights using the equation described as

$$\boldsymbol{w}(n+1) = \boldsymbol{w}(n) - \mu \frac{\partial e(n)}{\partial \boldsymbol{w}}, \tag{5}$$

where $\mu$ is the step size parameter which decides the learning speed and its stability. $\boldsymbol{w}$ represents all the weights in the ANN. The number of hidden layer units required to compensate for SPM is about ten or less [13]. The required number of input layer units, which is equal to the number of taps of the tapped delay line, is decided by the amount of CD [13].

### 2.2 VSTF-Based Nonlinear Equalizer

Figure 2 shows the VSTF-based nonlinear equalizer. Here, the Volterra kernels for the nonlinear compensation are acquired using the LMS algorithm. Optical nonlinearity of the optical fibers can be approximated by using only first- and third-order Volterra kernels [3], [4]. We omitted second-order Volterra kernels, because it is known that the second-order terms of the VSTF are not effective in equalizing the optical-fiber nonlinearity. The output of the VSTF is expressed as

$$y(n) = \sum_{m_1=-N}^{N} h_{m_1} x(n-m_1) + \sum_{m_1=-N}^{N} \sum_{m_2=m_1}^{N} \sum_{m_3=-N}^{N} h_{m_1 m_2 m_3} x(n-m_1)\, x(n-m_2)\, x^*(n-m_3), \tag{6}$$

where $x(n)$ and $y(n)$ are the real-valued input and real-valued output of the VSTF at time index, $n$, respectively, $h_{m_1}$ and $h_{m_1 m_2 m_3}$ are the first- and third-order Volterra kernels, respectively, and $L = 2N + 1$ expresses the number of taps of the tapped delay line. If we use only first-order Volterra kernels, omitting third- order terms in Eq. (6), the equalizer is equivalent to an FIR filter.

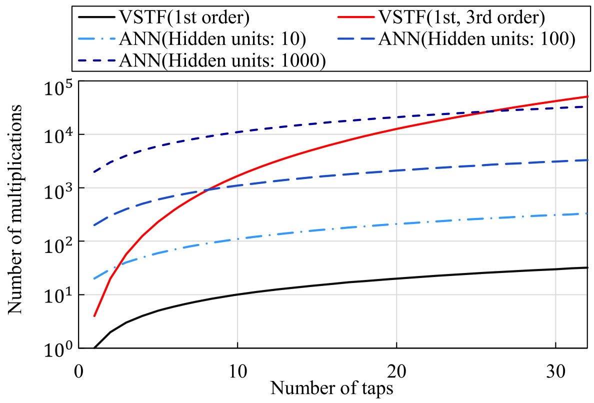


**Fig. 3** Required number of multiplications versus the number of taps.

### 2.3 Computational Complexity of ANN- and VSTF-Based Nonlinear Equalizers

The number of multiplications required for the ANN-based nonlinear equalizer to compensate for a symbol is expressed as

$$M_{\mathrm{ANN}} = L \times S_{\mathrm{hidden}} + S_{\mathrm{hidden}}, \tag{7}$$

where $M_{\mathrm{ANN}}$ is the number of real-valued multiplications, $L$ is the number of taps of the tapped delay line, and $S_{\mathrm{hidden}}$ is the number of hidden-layer units [14], [15]. Here, we neglect the calculations for the sigmoid functions of the hidden-layer units, assuming that a lookup table is employed. The number of real-valued multiplications required for a first-order VSTF (equivalent to an FIR filter) is expressed as

$$M_{\mathrm{VSTF(1st,order)}} = L. \tag{8}$$

The number of real-valued multiplications per symbol of first- and third-order VSTF-based nonlinear equalizers can be expressed as

$$\begin{aligned} M_{\mathrm{VSTF\,(1st,\,3rd\,order)}} &= L + 3L^2(L+1)/2 \\ &= \frac{3}{2}L^3 + \frac{3}{2}L^2 + L, \end{aligned} \tag{9}$$

where we eliminated the redundant terms, taking into account the symmetry of the Volterra kernels [14], [15]. Figure 3 shows the number of multiplications of the equalizers versus the number of taps. The number of multiplications in the ANN-based nonlinear equalizer increases linearly with the number of taps and hidden layer units. The number of multiplications in the first-order VSTF also increases linearly. On the other hand, for the first- and third-order VSTF, the number of multiplications increases in proportion to the cube of the number of taps. Therefore, if we need a long tapped delay line, the VSTF-based nonlinear equalizer will require significantly more multiplications than the ANN-based nonlinear equalizer.

## 3. System Setup for Evaluating Overfitting

Figure 4 shows the system setup used to evaluate the over-

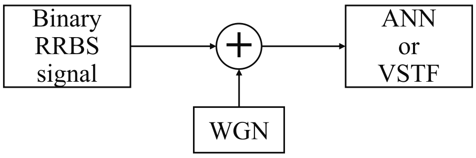


**Fig. 4** Additive WGN channel with RRBS.

fitting, which had been employed in previous studies on the overfitting evaluation of ANN-based nonlinear equalizers [16]–[18]. By employing this setup, we can simplify the evaluation to focus on the essential characteristics of the overfitting, eliminating the effects of the transmission parameters such as CD, SPM, pulse shape, and modulation formats. Even in actual transmission systems, the effects of the transmission parameters can be compensated by the equalizers, theoretically. Therefore, the essential characteristics of the overfitting are also applicable in actual transmission systems. A binary RRBS was generated by the Mersenne Twister (MT) algorithm. White Gaussian noise (WGN) was added to this binary baseband signal so that the signal-to-noise ratio (SNR) was adjusted to 4 dB. The bit lengths were changed from 15 to 31, 127, and 511 bits. The nonlinear equalizers were trained to try to “compensate” for the noise. The signal quality after the “compensation” was evaluated using the error vector magnitude (EVM). Essentially the noise cannot be compensated for using the equalizers. When the overfitting occurs, however, the equalizers predict the next incoming signals, resulting in an improvement of the apparent EVM values. The numbers of hidden-layer units of the ANN were 10, 100, and 1000. As noted in Sect. 2.1, only about ten or fewer hidden layer units are enough to compensate for the fiber nonlinearity [13]. Nevertheless, we attempted to use as many as 100 or 1000 hidden layer units to evaluate the overfitting characteristics of the ANN-based nonlinear equalizers with a computational complexity comparable to that of the VSTF. We employed the first-order VSTFs and the first- and third-order VSTFs. In the training of the ANN and VSTF, we did not employ the techniques such as batch normalization, a dropout layer, and an early stopping algorithm. This approach was chosen to compare the overfitting characteristics of ANN and VSTF in the simplest condition. This simplicity of the training algorithm is important in high-speed optical communication systems. We trained the equalizers over 100,000 epochs, which we confirmed to be a sufficient number of epochs. Each epoch involved the training and test samples with different noise generated using different seeds. We used the same RRBS generated using one seed through the training over 100,000 epochs to observe the overfitting to the RRBS. The numbers of the training and test samples correspond to the bit length of the RRBS used. The learning rate was adjusted to minimize the average learning error for each combination of the number of taps, the number of hidden units, and RRBS length.

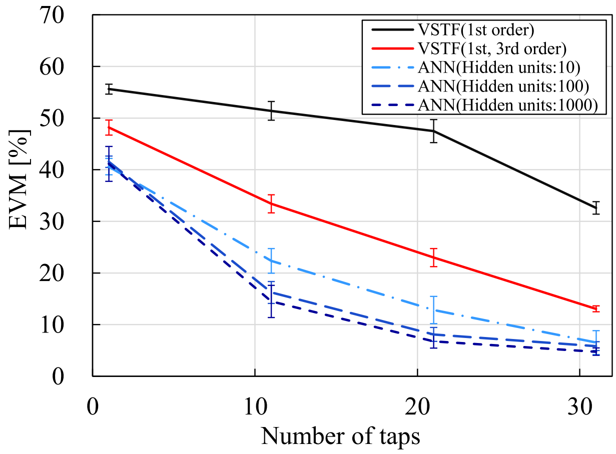


**Fig. 5** EVM versus the number of taps (trained on 15-bit RRBS).

## 4. Results and Discussion

First, we evaluated the overfitting with a short RRBS of 15 bits, which is comparable to or shorter than the number of taps of the tapped delay line of the nonlinear equalizers. 15 bits is impractically short, and it is easily expected that strong overfitting is prone to occur. However, we performed this investigation using the short RRBS to evaluate the overfitting of the first-order VSTFs (equivalent to FIR filters). Figure 5 shows the EVM versus the number of taps of the first-order VSTF-based nonlinear equalizer when trained on the 15-bit RRBS. In the figure, the characteristics of the first- and third-order VSTF and ANN are also presented for comparison. We plotted the averages of ten trials of the training, with the error bars representing the standard deviation at each tap length of the equalizers. The RRBSs for the ten trials were generated using different seeds. In the case of the first-order VSTF with one tap, the equalizer simply multiplies the input signal by a Volterra kernel. Therefore, the equalizer does not change the EVM of the input signal with WGN, and the value was about 55%. It should be noted that the EVM was decreased by overfitting when we increased the number of taps of the first-order VSTF. When the number of taps was as large as 31, the EVM was decreased by about 23%. In the case of the first- and third-order VSTFs and ANNs, the EVM values were decreased to about 48% and 41%, respectively, even when the number of taps was one. This is not due to the overfitting, but due to the clipping of WGN caused by the nonlinearity of the third-order terms of the VSTFs and the sigmoid functions of the ANNs.

Figure 6(a) shows the waveforms of the RRBSs with WGN before and after the first-order VSTF-based nonlinear equalizer with only one tap. As noted above, the equalizer simply multiplies the input signal by a Volterra kernel. Therefore, a linear relationship exists between the input and output waveforms. Figure 6(b) shows the waveforms before and after the first- and third-order VSTFs with one tap. In this case, we can observe that the amplitude of the WGN was clipped by the nonlinearity of the third-order terms of

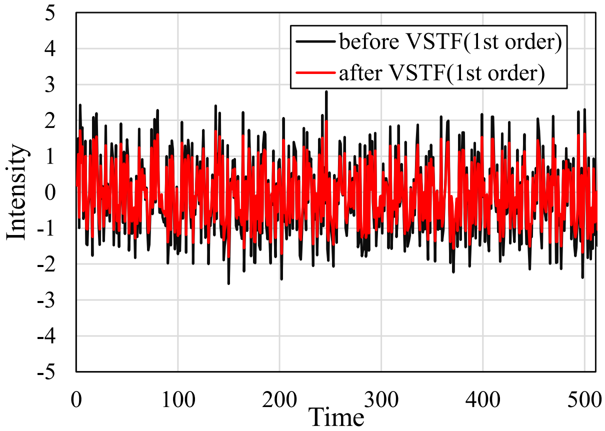

(a) First-order VSTF with one tap.

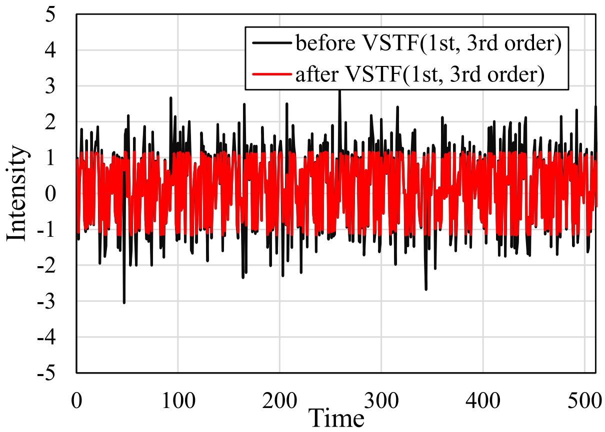

(b) First- and third-order VSTFs with one tap.

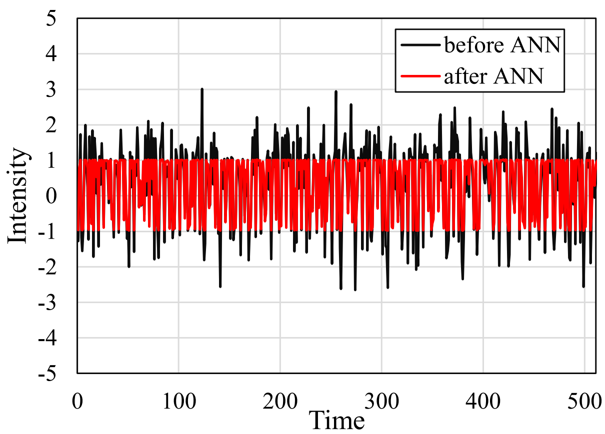

(c) ANN with one tap.

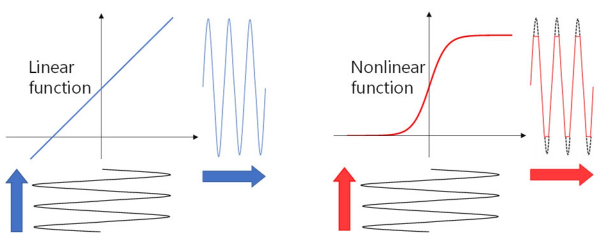

(d) Principle of clipping by nonlinearity.

**Fig. 6** Clipping of WGN by nonlinearity of equalizers.

the VSTF. When the overfitting is evaluated by using the EVM, we have to take into account the effect of the clipping caused by the nonlinearity of the equalizers. Figure 6(c) shows the waveforms before and after the ANN with ten hidden-layer units and one tap. The saturation curve of the sigmoid functions of the hidden-layer units causes stronger clipping than the VSTF. Figure 6(d) shows the principle of the clipping caused by the nonlinearity of the equalizers. When the transfer function of the equalizer is nonlinear, the large amplitude of the input signal is clipped to some extent, according to the nonlinear curve of the function. The first- and third-order VSTF-based nonlinear equalizers caused this clipping due to the nonlinear operation in the second term of Eq. (6), whereas the ANN-based nonlinear equalizers caused the clipping due to the nonlinearity of the activation function. These clippings decreased the apparent EVM, as shown in Fig. 5 and Fig. 6(b) and (c).

To eliminate the effects of the clipping, we plotted the variations in EVM, ΔEVM, from the value that was evaluated with one tap. Figure 7(a) is the replotted version of Fig. 5, showing the variations, ΔEVM, versus the number of taps of the VSTF- and the ANN-based nonlinear equalizers when trained on the 15-bit RRBS. In the case of the first-order VSTF, the EVM decreased by about 23% when the number of taps was 31, as mentioned above. When we used the first- and third-order VSTFs, the EVM decreased by about 35% with 31 taps, which shows larger overfitting than that which occurred in the case of the first-order VSTF. When we used the ANNs with 10, 100, and 1000 hidden-layer units, we observed stronger overfitting than observed with the VSTF. This result implies the high function representation capability of the ANN-based equalizers. However, when the number of taps was 31, the EVM decreased by about 35%, which was approximately equal to that of the first- and third-order VSTFs. This is due to the lower limit of the EVM, as shown in Fig. 5. Figure 7(b) shows ΔEVM versus the number of taps of the equalizers when trained on 31-bit RRBS. In the case of the first-order VSTF, the EVM decreased by 7% when the number of taps was 31. When we used the first- and third-order VSTFs, the EVM decreased by 27% with 31 taps. When we used the ANN with 10 hidden-layer units, the overfitting characteristics were comparable to those of the first- and third-order VSTFs. When we used the ANNs with 100 and 1000 hidden-layer units, we observed stronger overfitting than observed with the VSTF. This result shows the tendency toward weaker overfitting with an increase in the length of the RRBS used for the training. In order to investigate the overfitting characteristics with longer RRBS than the number of taps, we set the length to 127 bits. Figure 7(c) shows ΔEVM versus the number of taps of the equalizers which was trained on 127-bit RRBS. In the case of the first-order VSTF, EVM decreased by only 2% when the number of taps was 31, indicating the weak overfitting. When we used the first- and third-order VSTFs, the EVM decreased by 22% when the number of taps was 31. When we used the ANN with 10 hidden layer units, however, the EVM decreased by 7%, which is much smaller than that of the

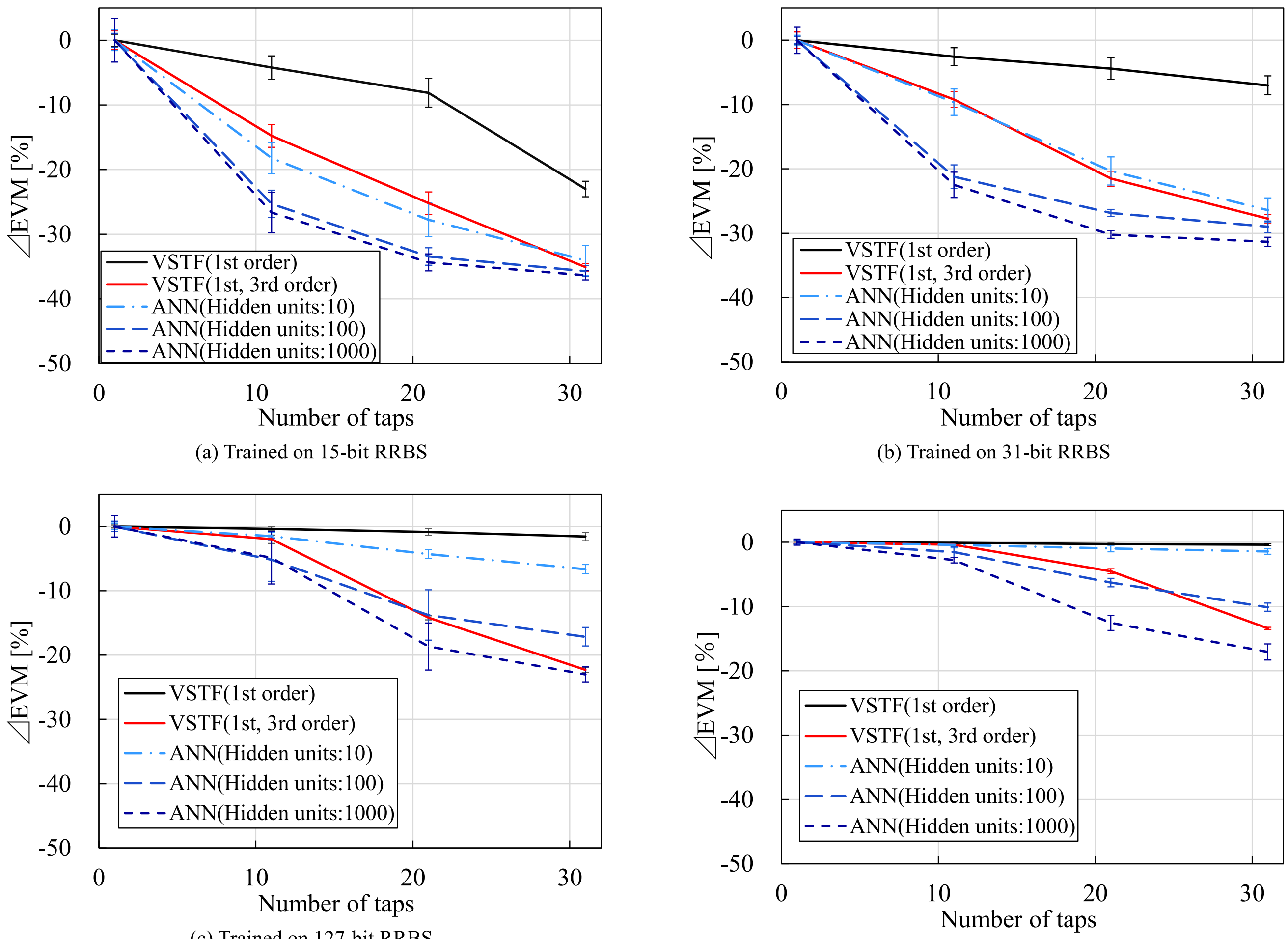


(a) Trained on 15-bit RRBS

(b) Trained on 31-bit RRBS

(c) Trained on 127-bit RRBS

(d) Trained on 511-bit RRBS

**Fig. 7** ΔEVM versus the number of taps.

first- and third-order VSTFs. When we used the ANNs with 100 and 1000 hidden-layer units, the overfitting characteristics were comparable to those of the first- and third-order VSTFs. Figure 7(d) shows ΔEVM versus the number of taps when a 511-bit RRBS was employed for the training. In the case of the first-order VSTF, the EVM variation was about 0%, even when the number of taps was as large as 31. When we used the first- and third-order VSTFs, the EVM decreased by 13%, when the number of taps was 31. On the other hand, when we used the ANN with 10 hidden-layer units, ΔEVM was only about 1%, even when the number of taps was as large as 31. In this case, the overfitting was suppressed enough, although we employed the ANN-based nonlinear equalizer. However, when we used the ANN and the number of hidden-layer units was as many as 100 and 1000, the overfitting characteristics were comparable to that of the first- and third-order VSTFs.

Figures 8(a) and (b) show the variations ΔEVM versus the bit length of the RRBS used for the training under the condition where the number of taps of the nonlinear equalizers was 31. First, we should note that the first-order VSTF, which is equivalent to an FIR filter, showed strong overfitting when the RRBS was as short as 31 or less. However, when the RRBS was longer than 127, the overfitting was sufficiently suppressed. In the case of the first- and third-order VSTFs, we observed strong overfitting, even when the RRBS was as long as 511. This result indicates that the first- and third-order VSTFs have a high function representation capability, and the VSTF-based nonlinear equalizer memorized the trained RRBS. Consequently, the equalizer predicted the incoming RRBS, and the EVM decreased. The ANN-based nonlinear equalizers have a high function representation capability as good as one based on the VSTF. However, when the number of hidden-layer units was as small as 10, the ΔEVM was only about 1%, and the overfitting was sufficiently suppressed against the 511-bit RRBS, whereas the first- and third-order VSTF showed strong overfitting in the same condition. As mentioned in Sect. 2.1, only about ten or fewer hidden layer units are sufficient to compensate for the fiber nonlinearity [13]. It should be noted that the computational complexity of the ANN-based nonlinear equalizer is much smaller than that of the VSTF, as shown in Fig. 3. However, when we increased the number of hidden-layer units to more than required, namely, 100 or 1000, we observed strong overfitting similar to the case of the VSTF. The results indicate that we need to carefully consider the overfitting and the

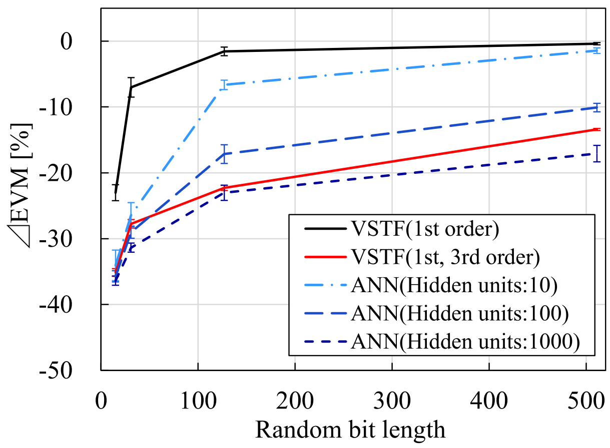


(a) Linear scale

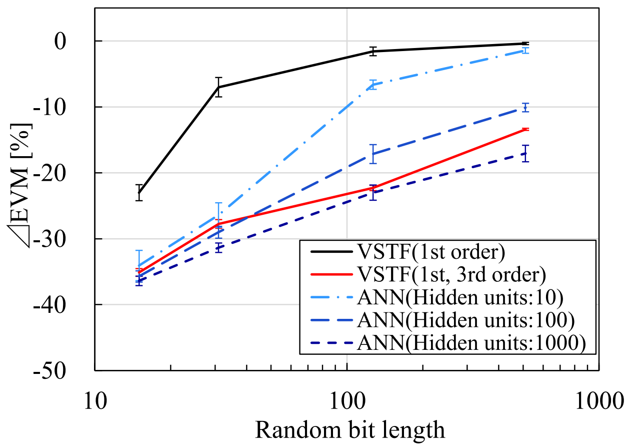


(b) Logarithmic scale

**Fig. 8** ΔEVM versus bit-length of RRBS.

required number of hidden-layer units of ANN-based nonlinear equalizers. In [22], the overfitting characteristics of the ANN- and VSTF-based nonlinear equalizers were compared using PRBSs. In this case, both equalizers showed stronger overfitting than what was observed in this study using RRBSs. This is because the ANN and VSTF can learn the simple generation rule of the PRBSs and consequently predict the received pattern. The overfittings of the nonlinear equalizers with RRBSs were weaker than that with PRBSs. In particular, when the number of the hidden-layer units of the ANN was as small as 10, the overfitting of the ANN was weaker than that of VSTF in the case of RRBSs.

## 5. Conclusion

We investigated the overfitting of ANN- and VSTF-based nonlinear equalizers trained on a finite-length RRBS. The results show that the VSTF used for nonlinear compensation in optical communication causes stronger overfitting than the ANN, depending on the conditions, in particular, the length of the RRBS and the number of taps. Nevertheless, it should be noted that we have to take care in deciding the number of hidden-layer units of the ANN. If we use more hidden-layer units than necessary, this will result in stronger overfitting. The problem of overfitting occurs not only with ANN-based nonlinear equalizers but also with general equalizers using learning algorithms. Depending on the conditions, the overfitting can occur even when we use a simple FIR filter.

## Acknowledgments

This work was supported by JSPS KAKENHI Grant Number 20K05367.

### References

[1] E. Ip and J.M. Kahn, "Compensation of dispersion and nonlinear impairments using digital backpropagation," J. Lightw. Technol., vol.26, no.20, pp.3416–3425, Oct. 2008. DOI: 10.1109/JLT.2008.927791
[2] L. Zhu, F. Yaman, and G. Li, "Experimental demonstration of XPM compensation for WDM fibre transmission," IET Electron. Lett., vol.46, no.16, pp.1140–1141, Aug. 2010. DOI: 10.1049/el.2010.1444
[3] Y. Gao, F. Zhang, L. Dou, Z. Chen, and A. Xu, "Intra-channel nonlinearities mitigation in pseudo-linear coherent QPSK transmission systems via nonlinear electrical equalizer," Optics Commun., vol.282, no.12, pp.2421–2425, June 2009. DOI: 10.1016/j.optcom.2009.03.002
[4] L. Liu, L. Li, Y. Huang, K. Cui, Q. Xiong, F.N. Hauske, C. Xie, and Y. Cai, "Intrachannel nonlinearity compensation by inverse Volterra series transfer function," J. Lightw. Technol., vol.30, no.3, pp.310–316, Feb. 2012. DOI: 10.1109/JLT.2011.2182038
[5] J. Estarán, R. Rios-Müller, M.A. Mestre, F. Jorge, H. Mardoyan, A. Konczykowska, J.-Y. Dupuy, and S. Bigo, "Artificial neural networks for linear and non-liner impairment mitigation in high-baudrate IM/DD systems," ECOC2016, M.2.B.2, Sept. 2016.
[6] S. Owaki, Y. Fukumoto, T. Sakamoto, N. Yamamoto, and M. Nakamura, "Experimental demonstration of SPM compensation based on digital signal processing using a three-layer neural-network for 40-Gbit/s optical 16QAM signal," IEICE Commun. Express, vol.7, no.1, pp.13–18, Jan. 2018. DOI: 10.1587/comex.2017XBL0148
[7] M.A. Jarajreh, E. Giacoumidis, I. Aldaya, S.T. Le, A. Tsokanos, Z. Ghassemlooy, and N.J. Doran, "Artificial neural network nonlinear equalizer for coherent optical OFDM," IEEE Photon. Technol. Lett., vol.27, no.4, pp.387–390, Feb. 2015. DOI: 10.1109/LPT.2014.2375960
[8] V. Kamalov, L. Jovanovski, V. Vusirikala, S. Zhang, F. Yaman, K. Nakamura, T. Inoue, E. Mateo, and Y. Inada, "Evolution from 8QAM live traffic to PS 64-QAM with neural-network based nonlinearity compensation on 11000 km open subsea cable," OFC2018, Th4D.5, March 2018.
[9] N. Kaneda, Z. Zhu, C.-Y. Chuang, A. Mahadevan, B. Farah, K. Bergman, D.V. Veen, and V. Houtsma, "FPGA implementation of deep neural network based equalizers for high-speed PON," OFC2020, T4D.2, March 2020.
[10] P.J. Freire, M. Anderson, B. Spinnler, T. Bex, J.E. Prilepsky, T.A. Eriksson, N. Costa, W. Schairer, M. Blott, A. Napoli, and S.K. Turitsyn, "Towards FPGA implementation of neural network-based nonlinearity mitigation equalizers in coherent optical transmission systems," ECOC2022, We1C.2, Sept. 2022.
[11] K. Liu, E. Börjeson, C. Häger, and P. Larsson-Edefors, "FPGA implementation of multi-layer machine learning equalizer with on-chip training," OFC2023, M1F.4, March 2023.
[12] M. Nakamura, Y. Fukumoto, S. Owaki, T. Sakamoto, and N. Yamamoto, "Experimental demonstration of SPM compensation using a complex-valued neural network for 40-Gbit/s optical 16QAM

signals," IEICE Commun. Express, vol.8, no.8, pp.281–286, Aug. 2019. DOI: 10.1587/comex.2019XBL0043

[13] M. Nakamura, Y. Fukumoto, and S. Owaki, "Size of an artificial neural-network for simultaneous compensation of linear and nonlinear optical waveform distortion," IEICE Commun. Express, vol.8, no.7, pp.269–274, July 2019. DOI: 10.1587/comex.2019XBL0049

[14] Y. Otsuka, Y. Fukumoto, S. Owaki, and M. Nakamura, "Computational-complexity comparison of artificial neural network and Volterra series transfer function for optical nonlinearity compensation," OECC2018, P1-25, July 2018.

[15] T. Kyono, Y. Otsuka, Y. Fukumoto, S. Owaki, and M. Nakamura, "Computational-complexity comparison of artificial neural network and Volterra series transfer function for optical nonlinearity compensation with time- and frequency-domain dispersion equalization," ECOC2018, Th2.28, Sept. 2018.

[16] T.A. Eriksson, H. Bülow, and A. Leven, "Applying neural networks in optical communication systems: possible pitfalls," IEEE Photon. Technol. Lett., vol.29, no.23, pp.2091–2094, Dec. 2017. DOI: 10.1109/LPT.2017.2755663

[17] L. Shu, J. Li, Z. Wan, W. Zhang, S. Fu, and K. Xu, "Overestimation trap of artificial neural network: Learning the rule of PRBS," ECOC2018, Tu4F.1, Sept. 2018.

[18] C.-Y. Chuang, L.-C. Liu, C.-C. Wei, J.-J. Liu, L. Henrickson, C.-L. Wang, Y.-K. Chen, and J. Chen, "Study of training patterns for employing deep neural networks in optical communication systems," ECOC2018, Tu4F.2, Sept. 2018.

[19] J. Kim and H. Kim "Length of pseudorandom binary sequence required to train artificial neural network without overfitting," IEEE Access, vol.9, pp.125358–125365, Sept. 2021. DOI: 10.1109/ACCESS.2021.3111092

[20] P.J. Freire, A. Napoli, B. Spinnler, N. Costa, S.K. Turitsyn, and J.E. Prilepsky, "Neural networks-based equalizers for coherent optical transmission: Caveats and pitfalls," IEEE J. Sel. Topics Quantum Electron., vol.28, no.4, art. seq. no.7600223, July/Aug. 2022. DOI: 10.1109/JSTQE.2022.3174268

[21] J. Nakamura, K. Ikuta, and M. Nakamura, "Overfitting characteristics of four-layer-deep-neural-network-based nonlinear equalizer for optical communication systems," IEICE Commun. Express, vol.11, no.7, pp.368–373, July 2022. DOI: 10.1587/comex.2022XBL0035

[22] K. Ikuta, Y. Otsuka, Y. Fukumoto, and M. Nakamura, "Overestimation problem with ANN and VSTF in optical communication systems," IET Electron. Lett., vol.55, no.19, pp.1051–1053, Sept. 2019. DOI: 10.1049/el.2019.2008

**Kai Ikuta** received the B.S. and M.S. degrees in Electrical Engineering from Meiji University, Kanagawa, Japan, in 2019 and 2021, respectively. In 2022, he became Research Associate with Meiji University, and is pursuing the D.E. degree. His research interests include optical communications and machine learning.

**Jinya Nakamura** received the B.S. and M.S. degrees in Electrical Engineering from Meiji University, Kanagawa, Japan, in 2021 and 2023, respectively. His research interests include optical communications and machine learning.

**Moriya Nakamura** received the B.E. and M.E. degrees in Electrical Engineering from Tokyo University of Science, Japan, in 1991 and 1993, respectively. He received the Ph.D. degree in Electrical Engineering from Osaka University, Japan in 2003. In 1993, he joined the Communications Research Laboratory, Ministry of Posts and Telecommunication (currently National Institute of Information and Communications Technology (NICT)). From 2013, he has been an Associate Professor with School of Science and Technology, Meiji University. He has been engaged in research and development of DSP-based linear and nonlinear equalization, coherent optical transmission, optical multi-level modulation, fiber-optic CDMA, and optical interconnection. He has served as a Program Officer of Basic Civilian Technologies in Telecommunications Advancement Organization (TAO), and as a Program Officer of SCOPE in the Ministry of Internal Affairs and Communications. He is a member of IEICE and IEEE.

PAPER

# Capacity and Reliability of Ionosphere Communication Channel Based on Multi-Carrier Modulation Technique and LUF-MUF Variation

**Varuliantor DEAR**[†,††a)], **Annis SIRADJ MARDIANI**[††], **Nandang DEDI**[††], **Prayitno ABADI**[†††,††††], ***Nonmembers***, **Baud HARYO PRANANTO**[†], ***Member***, ***and*** **ISKANDAR**[†], ***Nonmember***

**SUMMARY** Low capacity and reliability are the challenges in the development of ionosphere communication channel systems. To overcome this problem, one promising and state-of-the-art method is applying a multi-carrier modulation technique. Currently, the use of multi-carrier modulation technique is using a single transmission frequency with a bandwidth is no more than 24 kHz in real-world implementation. However, based on the range of the minimum and maximum ionospheric plasma frequency values, which could be in the MHz range, the use of these values as the main bandwidth in multi-carrier modulation techniques can optimize the use of available channel capacity. In this paper, we propose a multi-carrier modulation technique in combination with a model variation of Lowest Usable Frequency (LUF) and Maximum Usable Frequency (MUF) values as the main bandwidth to optimize the use of available channel capacity while also maintaining its reliability by following the variation of the ionosphere plasma frequency. To analyze its capacity and reliability, we performed a numeric simulation using a LUF-MUF model based on Long Short Term-Memory (LSTM) and Advanced Stand Alone Prediction System (ASAPS) in Near Vertical Incidence Skywave (NVIS) propagation mode with the assumption of perfect synchronization between transmitter and receiver with no Doppler and no time offsets. The results show the achievement of the ergodic channel capacity varies for every hour of the day, with values in the range of 10 Mbps and 100 Mbps with 0 to 20 dB SNR. Meanwhile, the reliability of the system is in the range of 8% to 100% for every hour of one day based on two different Mode Reliability calculation scenarios. The results also show that channel capacity and system reliability optimization are determined by the accuracy of the LUF-MUF model.
***key words:*** *ionosphere communication channel, capacity, reliability, multi-carrier, LUF, MUF*

## 1. Introduction

The main challenge of the ionospheric communication channel system is its low channel capacity and reliability. The low channel capacity is due to the multipath fading environment and the coherent bandwidth limitations [1], [2]. While the low-reliability main factor is caused by the boundary of the transmission frequency value, which follows the variation of the ionosphere plasma frequency [3]. To overcome the low capacity issue, a multi-carrier modulation technique such as Orthogonal Frequency Division Multiplexing (OFDM) is used as one of the solutions, with the purpose to avoid frequency selective fading [4]–[8]. To overcome the low reliability issue, a management frequency approach [9]–[11], along with the implementation of adaptive selection frequencies such as the Automatic Link Establishment (ALE) technique, employed in the system [12]–[14]. This technique enables the system to follow the variations in ionospheric plasma frequencies in order to guarantee the success of radio wave propagation from transmitter to receiver. Those approaches are known as the state-of-the-art methods in the development of the ionospheric communication channel system.

Currently, the use of a multi-carrier modulation technique in the ionosphere communication channel system uses a conventional main bandwidth which values are 3 kHz (narrowband HF) [15]–[19] and 24 kHz (wideband HF) [4], [20]–[22]. Meanwhile, the adaptive technique uses an analysis of data link quality from the sounding process to select a single frequency with a narrow bandwidth [23], [24]. Those combined approaches improve the reliability of the system by following the ionosphere plasma variation and increasing the channel capacity up to 9.6 kbps in the real-world implementation [25]. However, based on the range of minimum and maximum ionosphere frequency plasma values, which are in the range of MHz [3], [10], [26], the utilization of this frequency range as the main bandwidth of a multi-carrier modulation technique is quite promising. The utilization of the ionosphere frequency plasma range as the main bandwidth of the multi-carrier modulation technique could potentially optimize the use of available channel capacity while also maintaining its reliability. In this paper, we propose the multi-carrier modulation technique with a combination of the Lowest Usable Frequency (LUF) - Maximum Usable Frequency (MUF) variations in the ionosphere communication channel system and examine its capacity and reliability. The proposed system uses the variations of the LUF-MUF value from a model and uses it as the main bandwidth, where its maximum value could be more than

Manuscript received July 27, 2023.
Manuscript revised September 26, 2023.
Manuscript publicized January 30, 2024.
[†]The authors are with School of Electrical Engineering and Informatics, Institute Technology Bandung, Jl. Ganesha 20 West Java, Indonesia.
[††]The authors are with Space Research Center, National Research and Innovation Agency, Jl. Sangkuriang, Dago Bandung, Indonesia.
[†††]The author is with Research Center for Climate and Atmosphere, National Research and Innovation Agency, Jl. Sangkuriang Bandung, Indonesia.
[††††]The author is with School of Electrical Engineering, Telkom University, Kab. Bandung, Indonesia.
a) E-mail: varuliantor.dear@brin.go.id
DOI: 10.23919/transcom.2023EBP3122

10 MHz. For the sub-carrier bandwidth, the bandwidth coherent value based on the International Telecommunication Union's (ITU) recommendation is used, where its value is in the range of kHz [27]. To analyze its capacity and reliability, we performed a numeric simulation using a LUF-MUF model based on Long Short-Term Memory (LSTM) and Advanced Stand Alone Prediction System (ASAPS) for Near Vertical Incidence Skywave (NVIS) propagation mode. To get a comprehensive explanation, the structure of this paper is presented as follows: In Sect. 2 we discuss the variation of the ionosphere and its channel capacity and reliability calculation. In Sect. 3, we explain the main concept of the multi-carrier modulation technique with a combination of LUF-MUF variation and its capacity and reliability analysis method. In Sect. 4, we show and discuss the numerical simulation result. In the last section, we conclude this paper.

## 2. Theoretical Background

### 2.1 Variation of Ionosphere Channel

As a radio wave propagation medium in the High Frequency (HF) radio spectrum, the earth's ionosphere is formed by the electrons which resulted from atmosphere ionization at 60 to 2000 km altitudes. The formation of the ionosphere layers is determined by the space weather dynamics with the main source is solar activity radiation [28]. The dynamic formation of the ionosphere layer causes the frequency of radio waves that can propagate in the ionosphere layer to vary in time and place [3]. Variations of the radio wave frequency values that can be reflected by the ionosphere layer could refer to the critical frequency value of the ionospheric F layer ($f_oF2$) which has daily, seasonal, and solar cycle activity variations [28]. For application in ionospheric channel communication, the $f_oF2$ value can be converted into the lower limit and upper limit of reflected frequency, namely the Lowest Usable Frequency (LUF) and Maximum Usable Frequency (MUF). Therefore, to guarantee the propagation of radio waves from transmitter to receiver, the transmission frequency values should be selected between the LUF and MUF values.

The calculation of LUF and MUF is based on the geometry of the transmitter and receiver locations and is expressed by the equation as follows:

$$MUF = \alpha . f_oF2 \tag{1}$$

and

$$LUF = \alpha . f_{min} \tag{2}$$

with $\alpha$ is the geometry factors of transmitter and receiver locations which could be expressed using equations:

$$\alpha = \frac{\sqrt{h^2 + d^2}}{h} \tag{3}$$

$h$ is the height of the ionosphere layers, and $d$ is the distance between the transmitter and receiver. For Near Vertical Incidence Skywave (NVIS) propagation mode, where the distance of transmitter and receiver is less than 300 km, the value of $\alpha$ is equal to 1. The values of LUF and MUF directly follow the $f_{min}$ and $f_oF2$ values [29], [30].

### 2.2 Channel Capacity

Besides being known as a channel that has temporal and spatial variations, the ionosphere's physical properties also cause radio wave propagation from the transmitter to the receiver to experience more than one path, known as a multipath channel. As a multipath fading channel, ionospheric channel capacity can be calculated by the following equation:

$$C = \int_{-\infty}^{\infty} B \log_2(1 + \gamma) p(\gamma) d\gamma \tag{4}$$

where $C$ is the capacity in units of bits per second (bps). $B$ is the coherent bandwidth (Hz), $\gamma$ is the signal to noise ratio (SNR) value, and $p(\gamma)$ is the probability density function (pdf) of the SNR value, which follows the variation of the channel realization gain value. The channel capacity in the above equation is called the ergodic capacity, as it is known as a random process. For the upper limit of the channel capacity, the calculation using the Additive White Gaussian Noise (AWGN) channel could be used, which is expressed in the equation as follows:

$$C = B \log_2(1 + \overline{\gamma}) \tag{5}$$

with $\overline{\gamma}$ is the average of SNR. For the calculation of the total channel capacity using a multi-carrier modulation technique where each sub-channel is independent and identically distributed (i.i.d), the total ergodic capacity of the system could be expressed as follows:

$$C_{tot} = \Sigma_{k=1}^{K} B \log_2(1 + \gamma_k) p(\gamma_k) \tag{6}$$

with

$$\gamma_k = \frac{|g_k|^2 P_k}{N_k B_k} \tag{7}$$

$g$ is the realization of the channel gain for each of the $k$ sub-carriers, $P$ is the transmitted power, $N$ is the noise spectral density, and $B$ is the sub-carrier bandwidth with its values below the coherent bandwidth of the channel.

In addition to ergodic capacity, the calculation of multipath fading channel capacity can be expressed by outage capacity. Outage capacity is the probability of transmission failure based on specified criteria, such as minimum SNR. Outage capacity is expressed using the equation as follows:

$$C_{outage} = P_r(\log_2(1 + \gamma) < r) \tag{8}$$

where $Pr(.)$ is the probability function and $r$ is the minimum data rate threshold with an acceptable error value. Outage capacity also has meaning as a measure of system reliability.

### 2.3 Reliability of Ionosphere Communication System

To calculate the reliability of the ionospheric channel communication system, there are six types of reliability levels stated by the International Telecommunication Union (ITU) [31], namely: Mode Reliability, Circuit Reliability, Reception Reliability, Path Reliability, Communication Reliability, and Service Reliability. Mode Reliability (MR) is the basic level of ionospheric communication system reliability according to the limitations of the transmission frequency that could propagate in the skywave mode. In simple terms, the non-zero value of the Mode Reliability level is determined by the selection of the transmission frequency value in the range of LUF - MUF values. The Circuit Reliability is a calculation of communication circuit reliability based on the performance of a selected transmission frequency, such as the minimum SNR value limit. The Circuit Reliability calculation also includes the Mode Reliability calculation and is used as a basis for calculating the reliability level of a communication circuit, which is known as the Basic Circuit Reliability (BCR). For digital modulation, the BCR calculation is expressed by the equation as follows:

$$BCR(\%) = R_{SN}.R_T.R_F \tag{9}$$

where $R_{SN}$ is the probability of achieving the SNR minimum ($SN_o$). $R_T$ s the probability that the required time spread at a level of $-10$ dB relative to the peak signal amplitude is not exceeded. $R_F$ is the probability that the required frequency dispersion at a level of $-10$ dB relative to the peak signal amplitude is not exceeded. To calculate $R_{SN}$, there are two equations that could be selected based on the condition, which are:

$$\begin{aligned} R_{SN} &= 130 - 80/[1 + (SN_m - SN_o)/D_l] && \text{for } SN_m \geq SN_o \\ &= 80/[1 + (SN_o - SN_m)/D_u] - 30 && \text{for } SN_m < SN_o \end{aligned} \tag{10}$$

with $SN_m$ is the monthly median SNR value. $D_u$ and $D_l$ are the upper decile and lower decile deviation of monthly median SNR values, respectively. For calculating $R_T$, there are equations that are also based on two different conditions, which are:

$$\begin{aligned} R_T &= 130 - 80/[1 + (T_o - T_m)/D_{Tu}] && \text{for } T_m \leq T_o \\ &= 80/[1 + (T_m - T_o)/D_{Tl}] - 30 && \text{for } T_m > T_o \end{aligned} \tag{11}$$

with $T_m$ is the monthly median time spread, $D_{Tu}$ and $D_{Tl}$ are the lower decile and upper decile deviation of monthly median time spread values, respectively. For calculating $R_F$, the equations based on two conditions that could be used are:

$$\begin{aligned} R_F &= 130 - 80/[1 + (F_o - F_m)/D_{Fu}] && \text{for } F_m \leq F_o \\ &= 80/[1 + (F_m - F_o)/D_{Fl}] - 30 && \text{for } F_m > F_o \end{aligned} \tag{12}$$

where $F_m$ is the monthly median frequency dispersion,$D_{Fu}$ and $D_{Fl}$ are the upper decile and lower decile deviation of monthly median frequency dispersion values, respectively.

The $SN_m$, $R_T$, and $R_F$ values could be obtained from ionospheric physical models such as VOACAP [32]. While the upper and lower decile values for those parameters could be selected from the ITU document [31]. To determine the $SNo$ value, the BER curve as a function of SNR could be used based on the accepted minimum BER value.

For communication circuits that use more than one transmission frequency, the calculation of reliability is done using Basic Reception Reliability (BRR) which is expressed by the equation as follows:

$$BRR(\%) = 100[1 - \prod_{k=1}^{K}(1 - \frac{BCR(f_k)}{100})] \tag{13}$$

with $BCR(f_k)$ is the basic circuit reliability of each carrier frequency.

## 3. Multi-Carrier Modulation with LUF-MUF Variation

The basic form of multi-carrier modulation is dividing the data stream into multiple sub-streams that are transmitted over different orthogonal subchannels centered at different sub-carrier frequencies [33]. In this study, the proposed block diagram of the multi-carrier modulation technique with a combination of LUF-MUF variations in the ionosphere channel communication system is shown in Fig. 1. The data stream transmission is divided into an independent number of $K$ sub-carriers, which are determined by the variations of LUF-MUF and Bandwidth coherent ($B_c$) values. The values of LUF-MUF and $B_c$ are known on the transmitter and receiver sides.

The LUF and MUF values could be obtained from physics models such as the International Reference of Ionosphere (IRI) [34], the Advanced Stand-Alone Prediction System (ASAPS) [35], and NeQuick [36] that available for public uses. Those models are empirical models that were built using different methods but have a similar number of input variables, namely: location, time, and conditions of solar activity. In practice, more than one input variable could make the system more complex. Therefore, in addition to these empirical models, a method that is currently developing and has the potential to be used practically is a machine learning-based model [37]–[39]. The machine learning model could

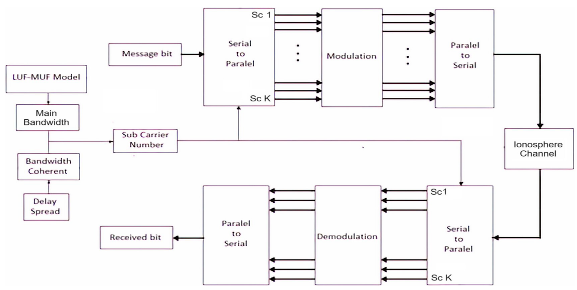


**Fig. 1** Block diagram of the proposed ionosphere communication system using the multi-carrier modulation technique and LUF-MUF variations. Variations of LUF-MUF values and bandwidth coherence determine the number of sub-carriers and are known by the transmitter and receiver for optimization of available capacity usage along with reliability.

utilize a single variable of time series data. Therefore, the LUF-MUF model based on machine learning is simpler to practically apply in the proposed system. In this study, the LSTM machine learning model was used for the analysis beside the empirical physic model namely ASAPS.

The LUF-MUF values determine the main bandwidth, with a value in the range of MHz. To roughly determine the number of sub-carriers of the proposed system, the main bandwidth is divided by the Bandwidth coherent ($B_c$) as spacing sub-carrier frequency to avoid frequency selective fading. The $B_c$ value is in the range of kHz and can be obtained from the delay spread value recommended by ITU [27] or from the channel sounding system as part of the channel estimation process [40], [41]. In this study, the $B_c$ value is 2 kHz refers to the ITU delay spread value in quite ionosphere conditions, and is known by the transmitter and receiver. To calculate the total channel capacity, the equation that could be used is expressed as follows:

$$C_{tot} = \Sigma_{k=1}^{K} B_k \log_2(1 + \frac{|g_k|^2 P_k}{N_k B_k}) \tag{14}$$

where $P_k$ is the transmit power, $g_k$ is the channel gain, $B_k$ is the sub-carrier bandwidth following the $Bc$ value, and $N_k$ is the noise spectral density values of each independent $k$ sub-carrier. The number of $K$ sub-carriers are determine using the following equations:

$$K_i = \frac{MUF_i - LUF_i}{B_c} \tag{15}$$

where $MUF - LUF$ is the value of the maximum-lowest usable frequency values as a function of time $i$, and $B_c$ is the coherent bandwidth value. In this calculation, the maximum number of sub-carriers is assumed without using guard band frequency and the system has perfect synchronization between transmitter and receiver with no Doppler, and no time offsets.

To calculate the reliability of the proposed system, the Basic Circuit Reliability (BCR) is used according to Eq. (9). However, because the ground truth of LUF-MUF determines the success of each sub-carrier frequency transmission in the BCR calculation, the Mode Reliability (MR) calculation should be conducted first. If the sub-carrier transmission frequency is outside the actual LUF-MUF range, then the transmission of radio waves from the transmitter to the receiver cannot be realized perfectly due to some sub-carrier frequencies not being reflected by the ionosphere [3], which inherently causes the BCR values for those frequencies to be zero. To calculate the Mode Reliability of the proposed multi-carrier technique, there are two scenarios that can be used, namely:

- Scenario #1. Transmission fails completely if one or more of the sub-carriers cannot be realized, and
- Scenario #2. Transmission can still be realized with some degree of reliability, even if some sub-carriers cannot be realized.

For the Scenario #1, the Mode Reliability (MR) calculation for multi-carrier transmission could be expressed as follows:

$$\begin{aligned} MR(\%) &= \frac{1}{M}\Sigma_{m=1}^{M} P(LUF;MUF)_m.100 \\ P(LUF;MUF)_m &= \begin{cases} 1, & \text{if } LUF_{pred} \geq LUF_{act} \\ & \cap MUF_{pred} \leqslant MUF_{act} \\ 0, & \text{otherwise} \end{cases} \end{aligned} \tag{16}$$

where MR is the Mode Reliability in the $M$ period time, $LUF_{pred}$ and $MUF_{pred}$ are the LUF and MUF from the model, and $LUF_{act}$ and $MUF_{act}$ are the actual values of LUF and MUF from observation. MR values that achieve 100% show that in periods of $M$, the system is reliable due to all sub-carrier transmissions being able to propagate in the ionosphere channel. However, if the MR value is less than 100%, then the system is not reliable at the period of $M$ because one or more sub-carrier transmissions are not able to propagate in the ionosphere channel. The $M$ period time could represent the period of an hour in one day or the period of a day in one month.

For the Scenario #2, where reliability is still realized even though there are several sub-carriers that fail to propagate in the ionosphere channel, the calculation of the Mode Reliability can be expressed by the equation:

$$\begin{aligned} MR(\%) &= \frac{\Sigma_{k=1}^{K} P(f_k)}{(\frac{MUF-LUF}{B_c})}.100 \\ P(f_k) &= \begin{cases} 1, & \text{if } LUF \leqslant f_k \leqslant MUF \\ 0, & \text{otherwise} \end{cases} \end{aligned} \tag{17}$$

where $B_c$ is the coherent bandwidth value which determines the number of sub-carriers from the main bandwidth. LUF-MUF is the actual value from the observation, and $P(f_k)$ is the probability of each $k$ sub-carrier frequency, which is in the range of the LUF-MUF from the model. In this scenario, even though one or more sub-carrier transmissions cannot be realized due to the ionospheric channel not supporting the propagation from the transmitter to the receiver, the system still has some degree of reliability.

## 4. Numerical Simulation Results

In this section we evaluate the ergodic capacity and reliability of the proposed system using numeric simulation. The simulation was done by sending a number of random message bits to each of the independent sub-carrier channels as shown in the block diagram of Fig. 1 and evaluating the achieved capacity and reliability. Parameter that used in the simulation are shown in Table 1, with assumption perfect synchronization between transmitter and receiver with no Doppler, and no time offsets which are source of Inter Symbol Interference (ISI) and Inter Carrier Interference (ICI). The sub-carrier frequencies are determined from the range of LUF-MUF values, which resulted from a model. For LUF-MUF models, we use the ASAPS and LSTM models.

**Table 1** Simulation parameter values.

| Parameter | Value | Description |
|---|---|---|
| Circuit location | Pontianak | 00.01.14;S 109.20.29;E |
| Propagation Mode | NVIS | |
| Actual LUF-MUF | Ionosonde CADI | Dec2022, Jan2023 |
| LUF-MUF Models | ASAPS and LSTM | Dec2022, Jan2023 |
| $SN_m$ | 40-50 dB | VOACAP |
| $SN_o$ | 24 dB | BPSK in Rayleigh |
| $B_c$ | 2 kHz | Normal condition |
| Number of bit | 10 Mbit | |
| Channel types | Rayleigh, AWGN | Ergodic, Upperbound |

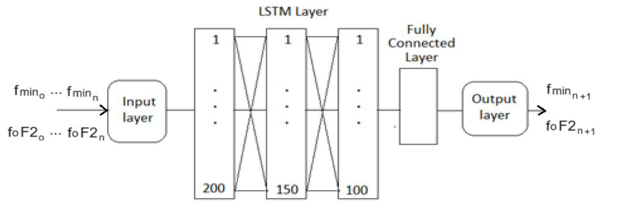


**Fig. 2** Architecture of the LSTM model to predict the LUF-MUF values.

The ASAPS model is provided in the public domain and could be used openly, with its prediction performance already reported in [42]–[44]. However, for the LSTM model, we designed its architecture and tested its performance.

## 4.1 LSTM Model Performance

Long short-term memory (LSTM) is an artificial neural network that has a feedback connection and thus can be classified as a recurrent neural network (RNN) [45]. LSTM has been shown to outperform traditional RNNs on numerous temporal processing tasks [46]. These temporal processing tasks include the processing of multivariate time-series data to perform predictions on future values. In this research, LSTM is used to predict the LUF-MUF values with the architecture of the LSTM model presented in Fig. 2.

The model of LSTM consists of three LSTM layers and one fully connected layer, with inputs in the form of $f_{min}$ and $f_oF2$ data set values. The data set was obtained from Ionosonde in Pontianak, and the period of data for the LSTM training and fitting process is December 2022. The output of the LSTM model is the prediction of the $f_{min}$ and $f_oF2$ values, and its performance is evaluated based on the actual $f_{min}$ and $f_oF2$ values from Ionosonde Pontianak in January 2023. The $f_{min}$ and $f_oF2$ prediction values are equivalent to the LUF-MUF values for determining the main bandwidth of the proposed system. The method of the LSTM model is open-loop forecasting, where the recent observation data is reused for the future prediction process.

The prediction results of the LSTM model for the parameters $f_{min}$ and $f_oF2$ as LUF-MUF equivalent values are presented in Fig. 3. Comparison of the predicted results of the LSTM model with the actual values shows that the root mean square error (RMSE) value is 0.55502 for the $f_{min}$ parameter. As for the parameter $f_oF2$, the RMSE value has reached 0.56099. The RMSE value of $f_{min}$ and $f_oF2$ that reaches 0.5 MHz will have a significant impact on the

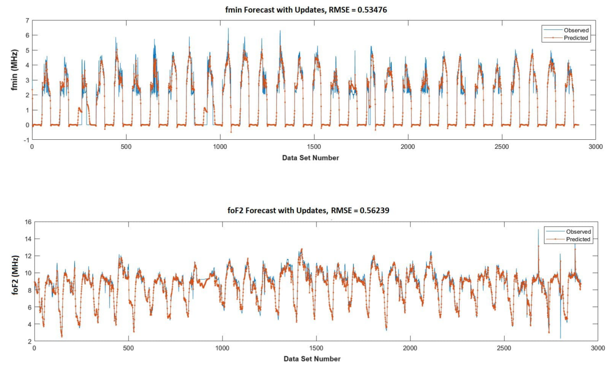


**Fig. 3** Comparison between predicted values output from the LSTM model and actual values for (a) $f_{min}$ and (b) $f_oF2$ in January 2023. The vertical axis is frequency, and the horizontal axis is the sequence of the predicted data set number.

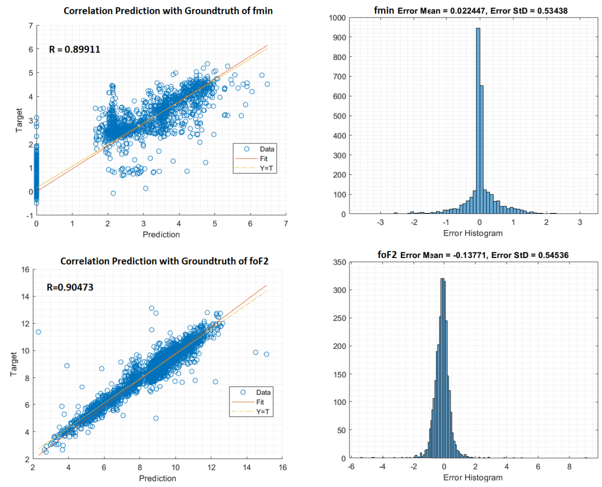


**Fig. 4** Performance of LSTM model for (a) $f_{min}$ and (b) $f_oF2$ prediction values.

utilization of available channels and the level of system reliability. For instance, using a 2 kHz bandwidth of subcarriers based on ITU delay spread recommendations values [27], the 0.5 MHz error prediction value lower than the actual could make around 250 subcarriers not used effectively. Meanwhile, the 0.5 MHz error prediction value higher than the actual could make around 250 subcarriers impossible to realize, which influenced the reliability of the system. Figure 4 shows the statistical analysis of the performance of the LSTM model. The correlation between the predicted results and the actual parameter $f_{min}$ is 0.89. As for the parameter $f_oF2$, the correlation is 0.905. The error distribution of $f_{min}$ has a mean 0.02247 and a standard deviation 0.53438. While the distribution of errors resulting from the prediction of $f_oF2$ has a mean value $-0.13771$ and a standard deviation of 0.54536.

## 4.2 Ergodic Channel Capacity

Figure 5(a) shows the results of calculating the ergodic capacity and upper limit (upper bound) of channel capacity

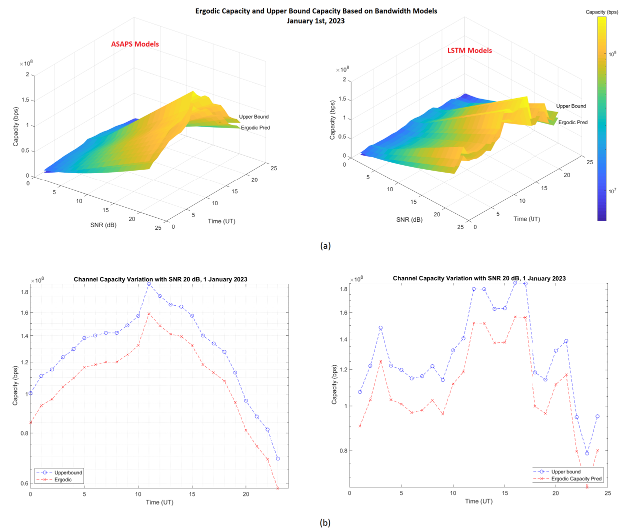


**Fig. 5** Comparison of ergodic capacity using the ASAPS and LSTM models on January 1, 2023, with (a) variations of SNR 1 to 20 dB and (b) SNR 20 dB. The achieved ergodic capacity values are in the range of $10^6$ to $10^8$ bps, while the conventional method is below $10^3$ bps [25].

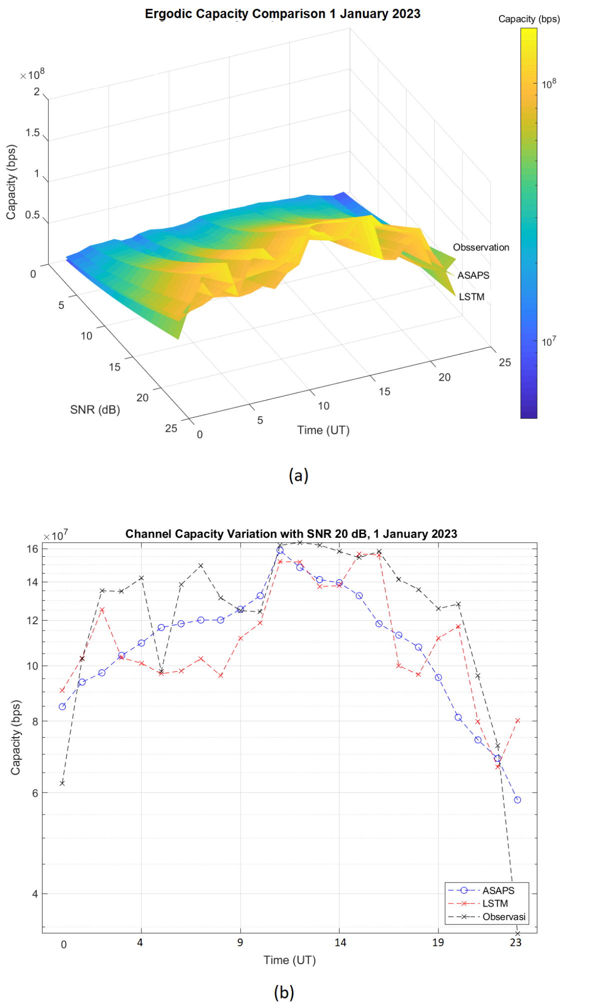


**Fig. 6** Calculation of the ergodic capacity based on the main bandwidth variations from the ASAPS model, LSTM model, and actual main bandwidth on January 1, 2023, with (a) variations of SNR from 1 to 20 dB and (b) SNR 20 dB.

on January 1, 2022, based on the main bandwidth values of the LUF-MUF ASAPS and LSTM models with SNR values between 1 and 20 dB. From the figure, it can be seen that the ergodic channel capacity varies every hour, with values ranging from 10 Mbps to 100 Mbps. This achieved ergodic capacity value is higher than the existing achieved capacity, which is 9.6 kbps [25].

In Fig. 5(b), it can be seen specifically the calculation of the ergodic capacity of the channel with 20 dB SNR of two model LUF-MUF. The channel ergodic capacity using the ASAPS model shows that the minimum ergodic capacity occurs at 23 Universal Time (UT), or 6 Local Time (LT; UT+7) with a value $5.8 \cdot 10^7$ bps. Meanwhile, the maximum capacity is at 12 UT or 19 LT, with values up to $1,58 \cdot 10^8$ bps. The minimum ergodic capacity using the LSTM is $6.6 \cdot 10^8$ bps and occurs at 22 UT or 05 LT. The maximum ergodic capacity of the LSTM model occurs at 15 UT or 22 LT with values up to $1.56 \cdot 10^8$ bps.

Figure 6 depicts a comparison of ergodic channel capacity between the ASAPS model, LSTM model, and the actual values on January 1, 2023. Figure 6(a) shows the calculation of ergodic channel capacity for SNR values between 1 and 20 dB. While Fig. 6(b) shows the ergodic channel capacity with 20 dB SNR. Based on the figure, it can be seen the difference between the ergodic channel capacity value of the model and the actual value. The calculation of ergodic channel capacity using models can be higher or lower than the actual ergodic channel capacity values. This condition depends on the comparison between the LUF-MUF values of the model and the actual LUF-MUF values, which determine the main bandwidth value. When the predicted main bandwidth value from the model is lower than the actual main bandwidth (an underestimate), there is still available ergodic channel capacity that can be realized. However, when the predicted main bandwidth from the model is higher than the actual main bandwidth (an overestimate), some ergodic channel capacity cannot be realized, which affects the system's reliability.

In Fig. 6(b), the actual ergodic capacity in the 23 UT to 00 UT, or 06 LT to 07 LT, is lower than the ergodic capacity of the ASAPS and LSTM models. This condition occurs due to the lower values of the actual main bandwidth compared to the predicted main bandwidth values from the ASAPS and LSTM models. The ASAPS and LSTM models exhibited limitations in accurately predicting the lower values of actual $f_{min}$ and $f_oF2$, consequently leading to higher main bandwidth and ergodic capacity when compared to the actual values. The inability of the ASAPS and LSTM models to predict the $f_{min}$ and $f_oF2$ could be attributed to the "sudden change" of the $f_{min}$ and $f_oF2$ trend values in those periods of time. Around 23 UT–00 UT, or 06–07 at local time, the sun begins to rise (sunrise). The formation of the ionosphere layers in this period changes from the dominant

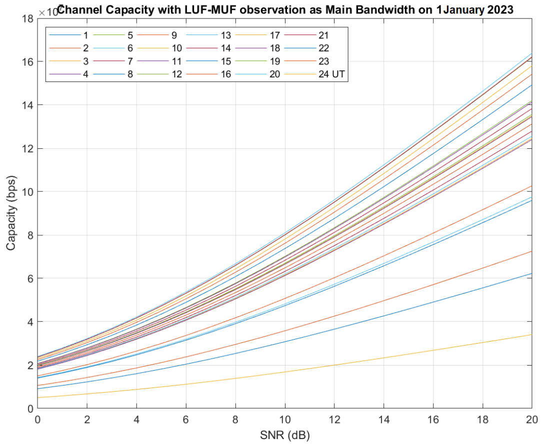


**Fig. 7** Ergodic channel capacity based on the actual bandwidth value of the ionosphere channel on January 1, 2023

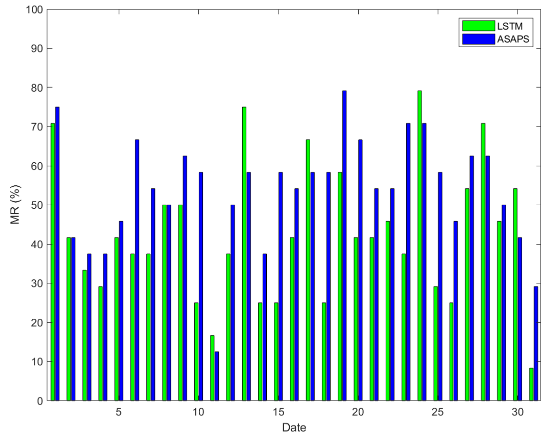


**Fig. 9** Mode reliability calculation result for each day in January 2023 using Scenario #1.

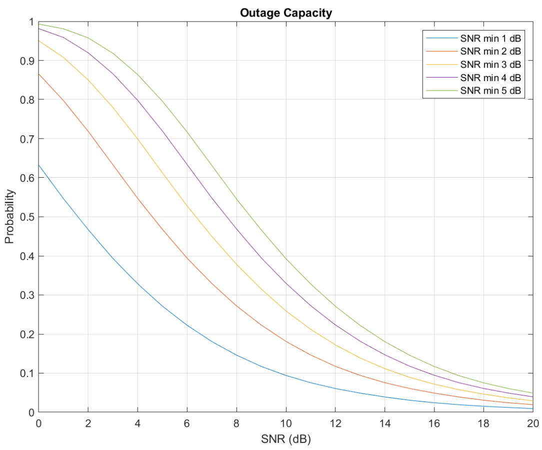


**Fig. 8** Outage capacity with minimum SNR ($SN_o$) from 1 to 5 dB.

recombination process to the dominant ionization process as the radiation from the sun starts [47]. The trends of the $f_{min}$ and $f_oF2$ values start to increase as the solar radiation increases, which is opposite to the previous trends. In addition to these conditions, the rate of the ionization process in the D layer, which determines the $f_{min}$ values, is different from the rate of the ionization process in the F layer, which determines the $f_oF2$ value [48]. The $f_{min}$ values increase faster than the $f_oF2$ values, which makes the actual main bandwidth lower compared to the previous values. These "sudden trend changes" could not be correctly predicted by the ASAPS and LSTM models, which resulted in a lower actual ergodic capacity value.

In Fig. 7, the calculation of ergodic channel capacity as a function of SNR for every hour on January 1, 2023, using the actual LUF-MUF value is presented. From the calculation results, it can be seen that the highest capacity occurs at 13 UT (20 LT) and the lowest capacity at 00 UT (07 LT). When the SNR is 0 dB, the difference in capacity between the minimum and maximum is 10 Mbps. Meanwhile, at 20 dB SNR, the difference reaches 100 Mbps.

In Fig. 8, the outage capacity with a minimum SNR value between 1 and 5 dB is presented as a general calculation of the reliability level of communication systems in the Rayleigh distributed channel. It can be seen that an increase in the SNR minimum or threshold value is followed by an increase in the outage capacity. If the SNR value on the receiving side increases and the minimum SNR value remains constant, the outage capacity value decreases.

### 4.3 Reliability

Figure 9 shows the calculation of the Mode Reliability for each day in January 2023 with the first scenario based on Eq. (16). The $M$ period of this Mode Reliability calculation is for each day in one month. From Fig. 9, it can be seen that the Mode Reliability using the LUF-MUF value from the ASAPS model in January 2023 is in the range of 10% to 79%, and the Mode Reliability using the LSTM model is in the range of 8% to 79%. The lowest value of Mode Reliability in the ASAPS model is 10%, which occurs on January 11, while the highest value of Mode Reliability is 79% and occurs on January 19. The lowest value of Mode Reliability of the LSTM model is 8% and occurs on January 31, while the highest value of Mode Reliability is 79% and occurs on January 24, 2023.

To get a more detailed explanation of calculation results from Mode Reliability values using Scenario #1, which is given in Fig. 9, a good example of comparative data between the LUF-MUF model values and the actual LUF-MUF values from observation over one day, namely January 6, 2023, is presented in Fig. 10. It can be seen that on January 6, 2023, between 11 and 22 UT, the LUF and MUF values of the ASAPS model are between the actual LUF-MUF values. This condition is considered reliable because the range of subcarrier frequencies that were selected in the transmission system could be realized. Different conditions occurred between 6 UT and 11 UT. The LUF-MUF value of the ASAPS model is outside the range of the actual LUF-MUF values, where the LUF model is lower than the actual LUF. Therefore, the system is considered unreliable because all the selected sub-

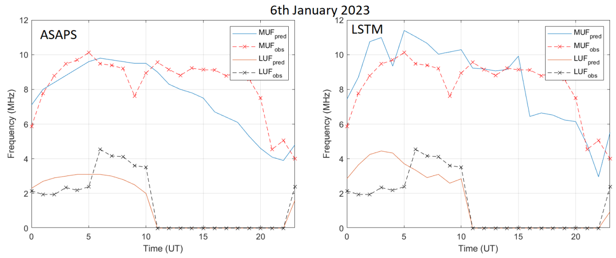


**Fig. 10** Comparison of actual LUF-MUF values with results from (a) ASAPS, and (b) LSTM models on 6th January 2023.

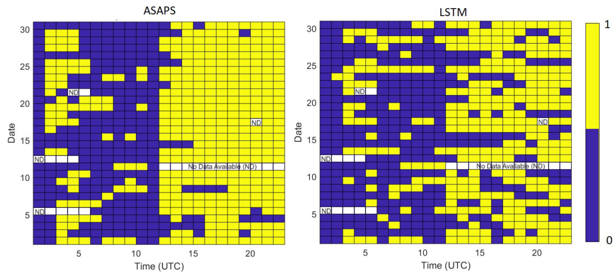


**Fig. 11** Mode reliability for each hour in January 2023 using Scenario #1. The yellow box color indicates the system is reliable. While the blue box color indicates the unreliability of the system, The white color with 'No Available Data (ND)' marks shows the unavailable MR calculation results due to the unavailable data of the actual LUF-MUF.

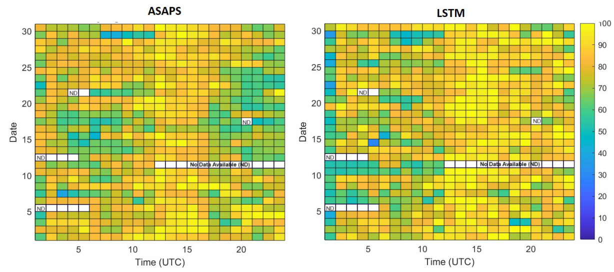


**Fig. 12** Mode Reliability for each hour in January 2023 using Scenario #2. The MR values are presented in color. The white color with 'No Available Data (ND)' marks shows the unavailable MR calculation results due to the unavailable data of the actual LUF-MUF.

carrier frequencies could not be fully realized. At different time periods, namely 0 UT to 1 UT, it can be seen that the predicted LUF value of the ASAPS model is within the range of actual LUF-MUF values. However, the predicted MUF value is outside the range of actual LUF-MUF values, which is considered to be an unreliable system. This condition explains why the ASAPS Mode Reliability value reached 68% on January 6, 2022, as shown in Fig. 9. Similar to the ASAPS model, some of the predicted LUF and MUF values from the LSTM models are within the range of the actual LUF-MUF values, which occurred between 16 and 22 UT, and are considered reliable. Meanwhile, the predicted LUF and MUF values between 6 UT and 10 UT were outside the range of the actual LUF-MUF values, which caused the system to be considered unreliable.

In Fig. 11, the Mode Reliability calculation result using the first scenario for every hour of every day in January 2023 based on Eq. (16) is presented. The $M$ period of this Mode Reliability calculation is for each hour in one day. The blue color represents a system considered unreliable, while the yellow color represents a system considered reliable. In every hour of the day, if the LUF-MUF from the model is within the range of the actual LUF-MUF, the system is considered reliable at that hour. However, if some values of the LUF-MUF from the model were outside the actual LUF-MUF, the system is considered not reliable at that hour due to the fact that one or more of the sub-carriers could not be realized. From the figure, it can be seen that the dominant reliable system occurs from 17 UT to 23 UT, which is at night in local time. The dominance of a reliable system at night can be attributed to the very low $f_{min}$ value parameter due to the disappearance of the D layer during nighttime [49]. With the disappearance of the D ionosphere layer, the determination of the main bandwidth only depends on the accuracy of the MUF value prediction.

Figure 12 is the second scenario Mode Reliability calculation result, which shows the hourly variations of MR values on each day in January 2023 for the ASAPS and LSTM models. For each hour in a day, there are no zero values for MR, which indicates the total failure of transmission. However, there are a number of hours for which the MR value cannot be calculated due to the unavailability of the actual LUF-MUF, which are on the 5th, 11th, 12th, 17th, and 21st. The unavailable MR calculation values are shown in a white color box with the 'No Available Data (ND)' mark. Based on the calculations, the Mode Reliability of the LSTM model shows a high value for each day from 12 UT to 20 UT, which reaches up to 100%. As for the ASAPS model, the highest value of Mode Reliability is in the range of 13 UT to 16 UT. The 100% value of Mode Reliability indicates that all sub-carrier transmissions based on the range of LUF and MUF model values are acceptable because the ionosphere layer is able to support the propagation. The Mode Reliability value that is less than 100% indicates that a number of sub-carrier transmissions fail due to being outside the range of the actual MUF-LUF value. Fluctuations in the Mode Reliability level indicate that transmission from each sub-carrier for every hour of the day cannot be fully realized. There are several sub-carrier transmissions experiencing problems as the LUF and MUF model values do not match the actual LUF and MUF values. The lowest value of the second scenario Mode Reliability calculation for both ASAPS and LSTM models is in the range of 40%.

The calculation of Mode Reliability in Fig. 12 shows the reliability fluctuations of the selected sub-carriers based on the realization of available sub-carriers. For each sub-carrier frequency that can be used, the BCR value can be calculated using equation (9) with monthly SNR ($SN_m$) values based on the VOACAP prediction model (Fig. 13(a)), $SN_o$ values based on the BER versus SNR curve using BPSK modulation (Fig. 13(b)) for BER values of $10^{-3}$, and $D_l$ values based on the ITU table (ITU, 1999). Using Eq. (9), the BCR value for a single sub-carrier frequency

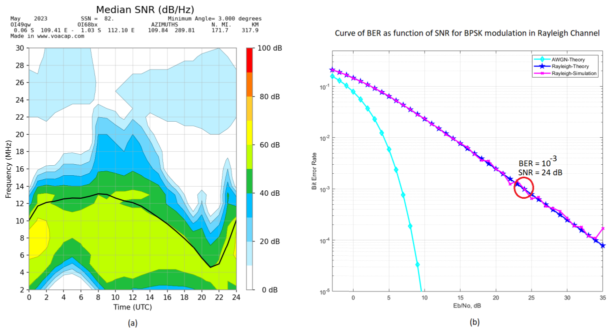


**Fig. 13** (a) Monthly SNR prediction from the VOACAP model, and (b) BER versus SNR curve for BPSK modulation in Rayleigh distributed channel. The $SN_o$ values can be determined based on acceptable BER values.

is $130 - 80/[1 + (50 - 24)/8].1.1 = 111.1765\%$ or 100%. Because the $SN_m$ value presented in Fig. 13(a) is quite uniform over the range of LUF-MUF values, this value can also be used as a representation of the BCR value for all sub-carrier frequencies, which is 100%. This result also affects the calculation of the BRR value using Eq. (13) with a 100% reliability. Even though the BRR value is 100%, it should be noted that this value is limited by the selection of the sub-carrier frequency in the range of the actual LUF-MUF value only. The LUF-MUF values from the model can be different from the actual LUF-MUF values. Therefore, the optimization of channel capacity and reliability in this system is determined by the accuracy factor of the LUF-MUF value model, whose function is the determination of the main bandwidth value.

## 5. Conclusion

The multi-carrier modulation technique, combined with LUF-MUF variation, is a promising method for improving the channel capacity while also maintaining the reliability of the ionospheric communication channel system. This method uses variations of LUF-MUF prediction values from a model as the main bandwidth and a Bandwidth coherent $B_c$ value as the subcarrier bandwidth. Numeric simulation using the ASAPS and LSTM models for the LUF-MUF values shows the achieved ergodic channel capacity varies in a range of 10 Mbps to 100 Mbps with SNR 0 to 20 dB. While the reliability level of the system using two scenarios of Mode Reliability calculation shows the values are in the range of 8% and 100% for every hour of the day. The simulation was conducted in Near Vertical Incidence Skywave (NVIS) propagation mode over the Pontianak region in January 2023 with the assumption of perfect synchronization, no Doppler, and no time offsets. The result also shows that the optimization of capacity and reliability were determined by the accuracy level of LUF-MUF models. If the model predicts lower LUF-MUF range values than the actual, the reliability level is maximized, but several of the available subcarrier bandwidths are not utilized. However, if the model predicts a higher LUF-MUF range value than the actual, the utilization of all the available subcarrier bandwidth is maximized, but sacrificing the reliability level to be low due to some of the sub-carrier transmissions cannot be realized.

## Acknowledgments

We would like to express our sincere gratitude to our supervisor, Professor Adit Kurniawan, for his valuable guidance and support throughout the research process. This work was supported by the Research Organization for Aeronautics and Space in DIPA 2023 for Space Research Center.

## References

[1] K. Davies, Ionospheric radio propagation, US Department of Commerce, National Bureau of Standards, 1965.
[2] S. Salous and L. Khadra, “Measuring the coherence of wideband dispersive channels,” Electron. Commun. Eng. J., vol.1, no.5, pp.205–209, 1989.
[3] N.M. Maslin, HF Communications: A Systems Approach, CRC Press, 2017.
[4] J.E. Nilsson and T.C. Giles, “Wideband multi-carrier transmission for military HF communication,” MILCOM 97 Proceedings, IEEE, 1997.
[5] H. Zhang, H. Yang, R. Luo, and S. Xu, “Design considerations of a new HF modem and performance analysis,” 2005 IEEE International Symposium on Microwave, Antenna, Propagation and EMC Technologies for Wireless Communications, pp.760–763, IEEE, 2005.
[6] J.W. Nieto, “An investigation of coded OFDM and OFDM-CDMA waveforms utilizing different modulation schemes on HF multipath/fading channels,” Proc. 2005 European Conference on Circuit Theory and Design, 2005, pp.III-65–68, IEEE, 2005.
[7] H. Chen and C. Jian, “Application research of technology combining AMC and OFDM in HF communication systems,” 2010 6th International Conference on Wireless Communications Networking and Mobile Computing (WiCOM), pp.1–6, IEEE, 2010.
[8] J.L. Pijoan, D. Altadill, J.M. Torta, R.M. Alsina-Pagès, S. Marsal, and D. Badia, “Remote geophysical observatory in antarctica with HF data transmission: A review,” Remote Sensing, vol.6, no.8, pp.7233–7259, 2014.
[9] G. Earl and B. Ward, “The frequency management system of the jindalee over-the-horizon backscatter HF radar,” Radio Science, vol.22, no.2, pp.275–291, 1987.
[10] J.M. Goodman, Space Weather & Telecommunications, Springer New York, NY, 2005.
[11] J. Wang, Y. Shi, C. Yang, and F. Feng, “A review and prospects of operational frequency selecting techniques for HF radio communication,” Advances in Space Research, vol.69, no.8, pp.2989–2999, 2022.
[12] R. Adair, “An automatic link establishment standard for automated digital HF radios,” IEEE Military Communications Conference,’Bridging the Gap. Interoperability, Survivability, Security’, pp.853–864, IEEE, 1989.
[13] W. Furman and E. Koski, “Next generation ALE concepts,” IET 11th International Conference on Ionospheric Radio Systems and Techniques (IRST 2009), pp.152–156, 2009.
[14] A. Haghbin, M. Khodaverdizadeh, and F. Razzazi, “Improving the performance of hf radio networks in presence of interference: Frequency hopping automatic link establishment,” 2022.
[15] Z. Zhang, F. Zeng, L. Ge, S. Chen, B. Yang, and G. Xuan, “Design and implementation of novel hf ofdm communication systems,” 2012 IEEE 14th International Conference on Communication Technology, pp.1088–1092, IEEE, 2012.
[16] A. Ismail and K. Mohamedpour, “Performance study of HF communication using NOMA over narrowband HF channel,” 2022.
[17] J. Nieto, “Constant envelope waveforms for use on HF multipath

fading channels," MILCOM 2008 — 2008 IEEE Military Communications Conference, pp.1–5, IEEE, 2008.
[18] M.F.G. Garcia, J.M. Paez-Borrallo, and S. Zazo, "Efficient pilot patterns for channel estimation in OFDM systems over HF channels," Gateway to 21st Century Communications Village. VTC 1999-Fall. IEEE VTS 50th Vehicular Technology Conference (Cat. no.99CH36324), pp.2193–2197, IEEE, 1999.
[19] P. Bechet, S. Miclaus, A. Miclaus, and C. Balint, "Experimental analysis of noise level and channels availability for high frequency OFDM data transmission in NVIS propagation conditions," 2016 International Symposium on Electromagnetic Compatibility-EMC EUROPE, pp.844–849, IEEE, 2016.
[20] C. Lamy-Bergot, A. Kermorgant, F. Gourgue, J.Y. Bernier, H. Diakhaté, and J.L. Rogier, "Wideband HF transmissions: Operating in a crowded spectrum," THALES Communications & Security, vol.92622, p.10, 2016.
[21] A.A. Ibrahim, A. Abdelaziz, and M.M. Salah, "On the performance of OFDM and single carrier communication over wideband HF channel: Theory and practice," Telecommun. Syst., vol.77, no.4, pp.671–682, 2021.
[22] A.A. Ibrahim, A.M. Abdelaziz, and M.M. Salah, "OFDM over wideband ionospheric HF channel: Channel modelling & optimal subcarrier power allocation," 2018 35th National Radio Science Conference (NRSC), pp.300–308, IEEE, 2018.
[23] Z. Qin, J. Wang, J. Chen, G. Ding, Y.D. Yao, X. Ji, and X. Chen, "Link quality analysis based channel selection in high-frequency asynchronous automatic link establishment: A matrix completion approach," IEEE Syst. J., vol.12, no.2, pp.1957–1968, 2017.
[24] R. Desourdis and E. Johnson, "Advanced link quality analysis for ALE HF radio," Proc. MILCOM'93-IEEE Military Communications Conference, pp.91–95, IEEE, 1993.
[25] W.N. Furman and J. Nieto, "Latest on-air testing of U.S. mil-std-188-110c appendix D wideband HF data waveforms," 12th IET International Conference on Ionospheric Radio Systems and Techniques (IRST 2012), 2012.
[26] C. Mudzingwa and A. Chawanda, "Radio propagation prediction for HF communications," Communications, vol.6, no.1, pp.5–12, 2018.
[27] ITU, "ITU-R REC. F.1487: Testing of HF modems with bandwidths of up to about 12 kHz using ionospheric channel simulators," International Telecommunication Union, Radiocommunication Sector, Geneva, 2000.
[28] L.F. McNamara, The Ionosphere: Communications, Surveillance, and Direction Finding, Krieger Publishing Company, 1991.
[29] M.C. Walden, "High-frequency near vertical incidence skywave propagation: Findings associated with the 5 MHz experiment," IEEE Antennas Propag. Mag., vol.58, no.6, pp.16–28, 2016.
[30] B.A. Witvliet and R.M. Alsina-Pagès, "Radio communication via near vertical incidence skywave propagation: An overview," Telecommun. Syst., vol.66, pp.295–309, 2017.
[31] I.T.U.R.S. (ITU-R), "Computation of reliability and compatibility of HF radio systems," 2007.
[32] A. Stocker, "Fast and accurate calculation of multipath spread from VOACAP predictions," Radio Science, vol.47, no.4, pp.1–10, 2012.
[33] A. Goldsmith, Wireless Communications, Cambridge University Press, 2005.
[34] D. Bilitza, "IRI the international standard for the ionosphere," Adv. Radio Sci., vol.16, pp.1–11, 2018.
[35] L.F. McNamara, C.R. Baker, and W.S. Borer, "Real-time specification of HF propagation support based on a global assimilative model of the ionosphere," Radio Science, vol.44, no.1, pp.1–13, 2009.
[36] S.M. Radicella and B. Nava, "Nequick model: Origin and evolution," Proc. 9th International Symposium on Antennas, Propagation and EM Theory, pp.422–425, IEEE, 2010.
[37] J. Wang, C. Yang, and W. An, "Regional refined long-term predictions method of usable frequency for HF communication based on machine learning over asia," IEEE Trans. Antennas Propag., vol.70, no.6, pp.4040–4055, 2021.
[38] M.A. Ameen, A. Tahir, M. Talha, H. Khursheed, I.A. Siddiqui, S.T. Iqbal, and B. Gul, "Modelling of $f_o F_2$ using artificial neural network over equatorial ionization anomaly (EIA) region stations," Advances in Space Research, vol.72, no.12, pp.5539–5550, 2023.
[39] R. Atıcı and Z. Pala, "Prediction of the ionospheric $f_o F_2$ parameter using R language forecasthybrid model library convenient time series functions," Wireless Pers. Commun., vol.122, no.4, pp.3293–3312, 2022.
[40] X. Tuo, W. Cheng, R. Yang, and H. Cheng, "The performance comparison of the channel estimation methods base on pilots symbol interpolation in HF OFDM system," 2015 3rd International Conference on Mechatronics and Industrial Informatics (ICMII 2015), pp.563–570, Atlantis Press, 2015.
[41] R.C. Cannizzaro, P. Banelli, and G. Leus, "Adaptive channel estimation for OFDM systems with Doppler spread," 2006 IEEE 7th Workshop on Signal Processing Advances in Wireless Communications, pp.1–5, IEEE, 2006.
[42] C. Brousseau, V. Gasse, and L. Bertel, "Comparison of three HF ionospheric prediction models (ASAPS, VOACAP, LOCAPI)," 8th International Ionospheric Effect Symposium, 1996.
[43] R. Barnes, R. Gardiner-Garden, and T. Harris, "Real time ionospheric models for the australian defence force," Proc. WARS-2000, vol.122135, pp.122–135, 2000.
[44] R. Malik, M. Abdullah, S. Abdullah, M.J. Homam, T. Yokoyama, and C. Yatini, "Prediction and measurement of high frequency radio frequencies in peninsular malaysia and comparisons with the international reference ionosphere model," Advanced Science Letters, vol.23, no.2, pp.1294–1298, 2017.
[45] S. Hochreiter and J. Schmidhuber, "Long short-term memory," Neural Computation, vol.9, no.8, pp.1735–1780, 1997.
[46] F.A. Gers, D. Eck, and J. Schmidhuber, "Applying LSTM to time series predictable through time-window approaches," International Conference on Artificial Neural Networks, pp.669–676, Springer, 2001.
[47] T. Yonezawa, "Theory of formation of the ionosphere," Space Sci. Rev., vol.5, no.1, pp.3–56, 1966.
[48] W. Webber, "The production of free electrons in the ionospheric $D$ layer by solar and galactic cosmic rays and the resultant absorption of radio waves," J. Geophysical Research, vol.67, no.13, pp.5091–5106, 1962.
[49] F. Gardner and J. Pawsey, "Study of the ionospheric D-region using partial reflections," Journal of Atmospheric and Terrestrial Physics, vol.3, no.6, pp.321–344, 1953.

**Varuliantor Dear** received the M.S. degrees in Electrical Engineering from Bandung Institute of Technology in 2015. Currently, he is a Doctor candidate in Bandung Institute of Technology and also works in the Space Research Center, National Institute and Innovation Agency Indonesia with research scope is the ionospheric channel propagation

**Annis Siradj Mardiani** received the B.S. degrees in Electrical Engineering from Achmad Yani University Indonesia, she works in the Space Research Center, National Institute and Innovation Agency Indonesia with research scope is the space weather impact to the ionosphere.

**Nandang Dedi** works at Space Research Center, National Institute and Innovation Agency Indonesia as a research assistant. His research scope is in Ionosphere Space weather information services.

**Prayitno Abadi** received his Doctorate degree from Nagoya University. Currently, he is a senior researcher at the Research Center for Climate and Atmosphere in the National Research and Innovation Agency of Indonesia, with research interests focusing on ionospheric effects on radio wave propagation. Additionally, he also serves as a lecturer for digital signal processing at Telkom University, Indonesia.

**Baud Haryo Prananto** received a B.S. degree from Bandung Institute and Technology, Indonesia in 2004 and M.S. degree from Korea Institute of Science and Technology, South Korea in 2008. Currently, he is studying at Bandung Institute of Technology as a Doctoral student. He is currently working as a Specialist Trainer in Nokia Solutions and Networks since 2008, delivering training related to 4G and 5G RAN Nokia equipment.

**Iskandar** received the M.S. and PhD degrees in Electrical Engineering from Bandung Institute of Technology and Waseda University, respectively. Currently, He is a lecture in Bandung institute of Technology.

IEICE TRANS. COMMUN., VOL.E107–B, NO.4 APRIL 2024

PAPER

# A Lightweight Graph Neural Networks Based Enhanced Separated Detection Scheme for Downlink MIMO-SCMA Systems*

**Zikang CHEN**[†,††], ***Student Member***, **Wenping GE**[†,††a)], **Henghai FEI**[†,††], **Haipeng ZHAO**[†,††], ***and*** **Bowen LI**[†,††], ***Nonmembers***

**SUMMARY** The combination of multiple-input multiple-output (MIMO) technology and sparse code multiple access (SCMA) can significantly enhance the spectral efficiency of future wireless communication networks. However, the receiver design for downlink MIMO-SCMA systems faces challenges in developing multi-user detection (MUD) schemes that achieve both low latency and low bit error rate (BER). The separated detection scheme in the MIMO-SCMA system involves performing MIMO detection first to obtain estimated signals, followed by SCMA decoding. We propose an enhanced separated detection scheme based on lightweight graph neural networks (GNNs). In this scheme, we raise the concept of coordinate point relay and full-category training, which allow for the substitution of the conventional message passing algorithm (MPA) in SCMA decoding with image classification techniques based on deep learning (DL). The features of the images used for training encompass crucial information such as the amplitude and phase of estimated signals, as well as channel characteristics they have encountered. Furthermore, various types of images demonstrate distinct directional trends, contributing additional features that enhance the precision of classification by GNNs. Simulation results demonstrate that the enhanced separated detection scheme outperforms existing separated and joint detection schemes in terms of computational complexity, while having a better BER performance than the joint detection schemes at high $E_b/N_0$ (energy per bit to noise power spectral density ratio) values.

***key words:*** *MIMO-SCMA, multi-user detection (MUD), bit error rate (BER), deep learning (DL)*

## 1. Introduction

### 1.1 Background

With the rapid development of the internet of things (IoT) [1], the demands placed on next generation wireless communication networks have become increasingly rigorous, requiring higher spectrum efficiency, reduced latency, and improved communication quality. While orthogonal multiple access (OMA) techniques have been successful in previous communication eras by mitigating inter-user interference through the allocation of orthogonal resource elements (REs) [2], the scarcity of spectrum resources driven by the pursuit of high throughput makes it challenging to rely solely on OMA techniques for resolution. The advent of non-orthogonal multiple access (NOMA) technology has revitalized the field of multiple access techniques, allowing for the transmission of signals from different users on the same RE, thereby increasing the overloading factor of REs to users and effectively alleviating the strain on limited spectrum resources [3].

Sparse code multiple access (SCMA) technology, as one of the various NOMA techniques, employs combinations of sparse code vectors, enabling simultaneous reception and decoding of multi-user signals [4]. This reduces the complexity of NOMA based systems while providing excellent anti-interference performance due to the high mutual information between different user signals. Multiple-input multiple-output (MIMO) technology, which utilizes spatial multiplexing, is another crucial technique for enhancing spectrum efficiency in next generation wireless communication networks [5].

In this context, MIMO-SCMA holds great promise in further improving spectrum efficiency, which is a primary reason for the sustained interest of the academic community in this field [6].

### 1.2 Related Work and Motivation

MIMO-SCMA is a technology that utilizes codebooks to map user data into multidimensional sparse codewords for transmission via multiple antennas. In order to improve the performance of MIMO-SCMA systems, a large-scale codebook optimization algorithm was proposed by [7]. Additionally, the design of the receiver plays a critical role in determining the performance of MIMO-SCMA systems. Separated detection algorithms, which combine MIMO detection algorithms [8] and SCMA detection scheme (message passing algorithm (MPA) [9]), suffer from inferior bit error rate (BER) performance and have a high computational complexity. To enhance the decoding performance, a joint sparse graph-detector that integrates the single graph of MIMO channels and SCMA codewords was proposed in [10]. However, while this technique effectively reduces the BER, it does not exhibit a significant decrease in computational complexity. Building upon the ideas presented in [10], [11] introduced two innovative low-complexity detectors based on an extended MIMO-SCMA factor graph for downlink MIMO-SCMA systems. The experimental results

Manuscript received August 23, 2023.
Manuscript revised October 23, 2023.
Manuscript publicized January 30, 2024.

[†]The authors are with College of Information Science and Engineering, Xinjiang University, 830046, China.
[††]The authors are also with the Signal Detection and Processing Key Laboratory, 830046, China.

*This work was partially supported by the Natural Science Foundation of Xinjiang Uygur Autonomous Region under Grant 2022D01C426 and supported by the Graduate Research Innovation Project of Xinjiang Uygur Autonomous Region under Grant XJ2023G100.

a) E-mail: wenpingge@xju.edu.cn

DOI: 10.23919/transcom.2023EBP3144

indicated that, while there was a noticeable reduction in computational complexity, there was a slight decline in BER performance. Therefore, existing separated and joint detection schemes do not achieve a balanced trade-off between computational complexity and BER performance.

Deep learning (DL) has become a widely utilized technology across various domains. In the SCMA systems, researchers in [12] applied DL to the receiver and developed a decoder with lower computational complexity than MPA while achieving a comparable BER performance. Building upon this work, [13] proposed an automatic encoder-decoder based on deep neural networks (DNNs) specifically designed for SCMA systems, demonstrating even lower computational complexity and superior BER performance. However, it is worth noting that these DL based SCMA decoders did not take into consideration the integration of SCMA with MIMO technology. [14] presented a DL based network model for application in the MIMO detection, thereby advancing the development of DL based MIMO-SCMA systems.

In this paper, we directly employ DL techniques for downlink MIMO-SCMA systems, and propose an enhanced separated detection algorithm based on lightweight graph neural networks (GNNS). We propose the concept of coordinate point relay, which maps the amplitude and phase of the estimated signal obtained by MIMO detection and the channel characteristics it have experienced into a $K$-point polyline graph with trend features. The differences in types of $K$-point polyline graphs can be ultimately attributed to the differences in the corresponding transmission symbol combinations. The GNNs all adopt the same modified MobileNet architecture [15]. Furthermore, we propose the concept of full-category training, where the utilized image dataset for the training process encompasses all categories of $K$-point polyline graphs, in contrast to the random training approach in [12]. This ensures a more scientific and rigorous training process. Our proposed scheme surpasses existing separated and joint detection schemes in terms of computational complexity, while achieving a better BER performance than the joint detection schemes across the high $E_b/N_0$ (energy per bit to noise power spectral density ratio) values.

### 1.3 Contributions

- We propose the concept of coordinate point relay, which allows us to generate $K$-point polyline graphs with trend features for training purposes. The eigenvalues of the $K$-point polyline graphs contain crucial information, including the amplitude and phase of estimated signals, as well as channel characteristics. Additionally, different types of $K$-point polyline graphs exhibit diverse trend directions, providing extra features that aid in accurate classification by the GNNs.
- We propose the concept of full-category training, whereby the employed image dataset for training comprises all distinct categories of $K$-point polyline graphs. This approach guarantees a more methodical and rigorous training process, lending greater scientific validity to our study.
- Our proposed algorithm presents a novel research perspective by combining traditional communication and computer vision techniques. This approach offers a fresh insight into multi-user detection (MUD) in the downlink MIMO-SCMA system, by replacing the role of the MPA at the SCMA receiver with image classification techniques based on lightweight GNNs. Additionally, our algorithm balance both computational complexity and BER performance. In comprehensive evaluations, it demonstrates superior performance compared to existing separated and joint detection schemes.

### 1.4 Organization

The remainder of this article is organized as follows. Section 2 introduces the downlink MIMO-SCMA system model. Section 3 introduces the conventional separated detection scheme, and describes our lightweight GNNs based enhanced separated detection scheme (LG-ESDS) in detail. Section 4 presents and evaluates the simulation results. Finally, Sect. 5 presents the conclusions.

## 2. Downlink MIMO-SCMA System Model

Figure 1 illustrates a downlink MIMO-SCMA system with $J$ independent users multiplexed over $K$ orthogonal REs, achieving an overloading factor of $\lambda = J/K$. In this system, the base station is equipped with $N_t$ transmit antennas, while each user is equipped with $N_r$ receive antennas. For the $n_t$-th antenna of user $u$, where $n_t = 1, 2, \ldots, N_t$ and $u = 1, 2, \ldots, J$, the input $\log_2(M)$ binary bits $\mathbf{b}_u^{n_t}$ are mapped into a $K$-dimensional complex codeword $\mathbf{x}_u^{n_t} = \left[x_{u,1}^{n_t}, x_{u,2}^{n_t}, \ldots, x_{u,K}^{n_t}\right]^T$, which is selected from the known corresponding SCMA codebook $\mathrm{C}_u^{n_t} \in \mathbb{C}^{K\times M}$ with size $M$. Based on the size of the codebook, each user can be considered to have $M$ possible transmission symbols (e.g., $0, 1, \ldots, M-1$). Therefore, at the $n_t$-th antenna, the transmitted overlapping codeword corresponding to the transmission symbols combination (TSC) of $J$ users can be represented

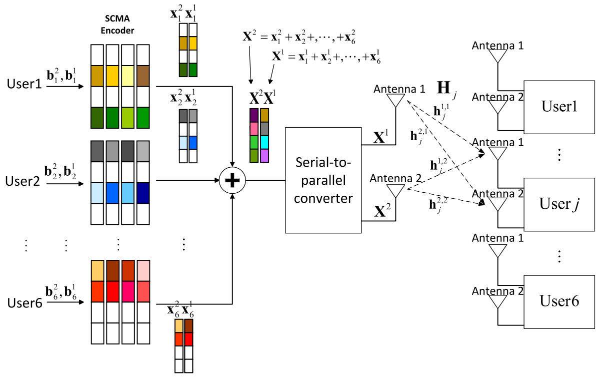


**Fig. 1** Architecture of downlink MIMO-SCMA system with $J$ = 6, $K$ = 4, $M$ = 4, $N_t$ = 2, and $N_r$ = 2.

as

$$\mathbf{x}^{n_t} = \sum_{u=1}^{J} \mathbf{x}_u^{n_t}. \tag{1}$$

The received signal at the $n_r$-th antenna of user $j$, where $j = 1, 2, \ldots, J$ and $n_r = 1, 2, \ldots, N_r$, can be expressed as

$$\mathbf{y}_j^{n_r} = \sum_{n_t=1}^{N_t} \operatorname{diag}\left\{\mathbf{h}_j^{n_r,n_t}\right\} \mathbf{x}^{n_t} + \mathbf{n}_j^{n_r}, \tag{2}$$

where $\mathbf{h}_j^{n_r,n_t} = \left[h_{j,1}^{n_r,n_t}, h_{j,2}^{n_r,n_t}, \ldots, h_{j,K}^{n_r,n_t}\right]^T$ represents the channel gain vector between the $n_t$-th antenna of base station and the $n_r$-th antenna of $j$-th user, and $\mathbf{n}_j^{n_r} = \left[n_{j,1}^{n_r}, n_{j,2}^{n_r}, \ldots, n_{j,K}^{n_r}\right]^T$ is the additive white Gaussian noise (AWGN) with zero mean and variance $\sigma_{n_r}^2$. By stacking the signals at all $N_r$ receive antennas together, we can obain the received signal $\mathbf{y}_j$ of user $j$, which can be expressed as

$$\mathbf{y}_j = \sum_{n_t=1}^{N_t} \sum_{u=1}^{J} \operatorname{diag}\left\{\mathbf{h}_j^{n_t}\right\} \tilde{\mathbf{x}}_u^{n_t} + \mathbf{n}_j, \tag{3}$$

where

$$\begin{aligned}
\mathbf{y}_j &= \left[\left(\mathbf{y}_j^1\right)^T, \left(\mathbf{y}_j^2\right)^T, \ldots, \left(\mathbf{y}_j^{N_r}\right)^T\right]^T, \\
\mathbf{h}_j^{n_t} &= \left[\left(\mathbf{h}_j^{1,n_t}\right)^T, \left(\mathbf{h}_j^{2,n_t}\right)^T, \ldots, \left(\mathbf{h}_j^{N_r,n_t}\right)^T\right]^T, \\
\tilde{\mathbf{x}}_u^{n_t} &= \left[\left(\mathbf{x}_u^{n_t}\right)^T, \left(\mathbf{x}_u^{n_t}\right)^T, \ldots, \left(\mathbf{x}_u^{n_t}\right)^T\right]^T, \\
\mathbf{n}_j &= \left[\left(\mathbf{n}_j^1\right)^T, \left(\mathbf{n}_j^2\right)^T, \ldots, \left(\mathbf{n}_j^{N_r}\right)^T\right]^T.
\end{aligned} \tag{4}$$

## 3. Separated Detection Scheme for Downlink MIMO-SCMA System

In Sect. 3.1, we commence by introducing the concept of conventional separated detection algorithm. Following that, we present a comprehensive and detailed exposition of our novel LG-ESDS in Sect. 3.2.

### 3.1 Conventional Separated Detection Algorithm

Figure 2 illustrates the architecture of the conventional separated detection algorithm, depicting four distinct categories of nodes. These categories include RA nodes representing the receive antennas, TA nodes denoting the transmit antennas, R nodes embodying the REs, and U nodes signifying the users. The conventional separated detection algorithm refers to a two-step process, involving MIMO detection followed by MPA decoding of the estimated signals obtained from MIMO detection. During this process, MIMO detection and MPA decoding are performed independently. However, MPA necessitates numerous iterative loops, which hinders meeting the low latency requirements of modern communication systems. Moreover, MPA relies on continuous message exchange between R nodes and U nodes, resulting in the transmission and reception of both relevant and irrelevant information. This makes it difficult to directly exploit the effective information of the estimated signals. In light of this, we propose the LG-ESDS for MIMO-SCMA systems.

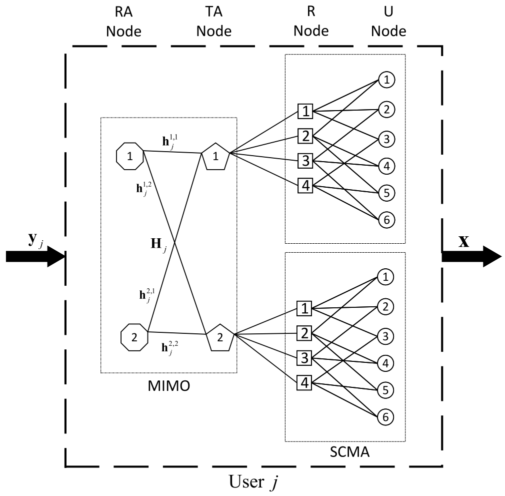


**Fig. 2** Architecture of conventional separated detection algorithm with $J = 6$, $K = 4$, $M = 4$, $N_t = 2$, and $N_r = 2$.

### 3.2 LG-ESDS

In Sect. 3.2.1, we provide an introduction to the MIMO detection algorithm: minimum mean square error (MMSE) detectionn algorithm [8], which is utilized in our proposed LG-ESDS. In Sect. 3.2.2, we provide a detailed description of the concept of coordinate point relay, which enables the replacement of MPA in SCMA decoding with GNNs based image classification technology. Moving to Sect. 3.2.3, we propose the concept of full-category training to enhance the scientific and rigorous nature of the training process. Then, we elucidate the logical derivation for optimizing GNNs parameters. Section 3.2.4 focuses on the experimental setup and parameter configuration employed in our simulation experiment. We present the model parameters of the MIMO-SCMA system used and describe the specific structure of the GNNs. Moreover, we outline the parameter settings of our proposed LG-ESDS. While the detection scheme we have proposed can be applied to larger MIMO-SCMA systems, it is important to note that the design of codebooks for such systems falls outside the scope of our study. Therefore, we consider a downlink MIMO-SCMA system where different transmit antennas employ the same mapping codebook. Based on this, we only need to clarify how our proposed LG-ESDS helps user $j$ retrieve his own information transmitted by the antenna $n_t$.

#### 3.2.1 MMSE Detection Algorithm

Based on Eqs. (3), a more simplified representation of $\mathbf{y}_j$ can be achieved as

$$\mathbf{y}_j = \mathbf{H}_j\mathbf{x} + \mathbf{n}_j, \tag{5}$$

where $\mathbf{H}_j = \left[\mathbf{h}_j^1, \mathbf{h}_j^2, \ldots, \mathbf{h}_j^{N_t}\right]$ is the MIMO channel matrix, $\mathbf{x} = \left[\left(\mathbf{x}^1\right)^T, \left(\mathbf{x}^2\right)^T, \ldots, \left(\mathbf{x}^{N_t}\right)^T\right]^T$, and $\mathbf{n}_j$ is the complex Gaussian noise vector at $j$-th user with zero mean and variance $\sigma^2$.

The fundamental principle of the MMSE algorithm is to minimize the expected value of the mean square error between the estimated signal and the actual transmitted signal [8]. Mathematically, this can be expressed as follows:

$$F_{MMSE} = \arg\min_F E\left\|F\mathbf{y}_j - \mathbf{x}\right\|^2, \tag{6}$$

where $F_{MMSE}$ is defined as the objective function of the MMSE algorithm. According to the principle of orthogonality, we can derive

$$E\left\{\left(F_{MMSE}\mathbf{y}_j - \mathbf{x}\right)\mathbf{y}^H\right\} = 0, \tag{7}$$

where $\mathbf{y}^H$ is the conjugate transpose of $\mathbf{y}_j$. By combining Eqs. (5) and (7) and employing the principle of matrix inversion, we can obtain the simplified expression

$$F_{MMSE} = \left(\mathbf{H}_j^H\mathbf{H}_j + \sigma^2\mathbf{I}_K\right)^{-1}\mathbf{H}_j^H, \tag{8}$$

where $\mathbf{H}_j^H$ is the conjugate transpose of $\mathbf{H}_j$, and $\mathbf{I}_K$ is a $K$-dimensional identity matrix. Therefore, the estimated signal $\mathbf{e}$ obtained through the MMSE algorithm can be represented as

$$\mathbf{e} = F_{MMSE}\mathbf{y}_j = \left(\mathbf{H}_j^H\mathbf{H}_j + \sigma^2\mathbf{I}_K\right)^{-1}\mathbf{H}_j^H\mathbf{y}_j, \tag{9}$$

where $\mathbf{e} = \left[\left(\mathbf{e}^1\right)^T, \left(\mathbf{e}^2\right)^T, \ldots, \left(\mathbf{e}^{N_t}\right)^T\right]^T$, and $\mathbf{e}^{n_t} = \left[e_1^{n_t}, e_2^{n_t}, \ldots, e_K^{n_t}\right]^T$ represents the estimated value of the signal transmitted by the antenna $n_t$.

### 3.2.2 Coordinate Point Relay

The realization of the coordinate point relay is accomplished in the PyTorch environment, utilizing the matplotlib module [16]. We map the first component, $e_1^{n_t}$, of $\mathbf{e}^{n_t}$, including both the real and imaginary parts (i.e., $\mathrm{Re}\left(e_1^{n_t}\right)$ and $\mathrm{Im}\left(e_1^{n_t}\right)$), onto a Cartesian coordinate system, resulting in the coordinate point $c_1$, which can be expressed as

$$(X_1, Y_1) = \left(\mathrm{Re}\left(e_1^{n_t}\right), \mathrm{Im}\left(e_1^{n_t}\right)\right), \tag{10}$$

where $(X_1, Y_1)$ represents the coordinate of $c_1$. Based on this, we can obtain the corresponding point $c_2$ in the Cartesian coordinate system for the second component, $e_2^{n_t}$, of $\mathbf{e}^{n_t}$, that can be expressed as

$$(X_2, Y_2) = (X_1, Y_1) + \left(\mathrm{Re}\left(e_2^{n_t}\right) + \mathrm{RF}, \mathrm{Im}\left(e_2^{n_t}\right)\right), \quad \mathrm{Re}\left(e_2^{n_t}\right) + \mathrm{RF} > 0, \tag{11}$$

where $(X_2, Y_2)$ represents the coordinate of $c_2$, $\mathrm{Re}\left(e_2^{n_t}\right)$ and $\mathrm{Im}\left(e_2^{n_t}\right)$ represent the real and imaginary parts of $e_2^{n_t}$, and RF is the rightwalk factor (RF), which is a novel concept proposed by us, ensuring that $c_2$ lies to the right of $c_1$. Similarly, we can obtain the corresponding points in the Cartesian coordinate system for the remaining $K-2$ components of $\mathbf{e}^{n_t}$. This can be expressed as

$$(X_{z+1}, Y_{z+1}) = (X_z, Y_z) + \left(\mathrm{Re}\left(e_{z+1}^{n_t}\right) + \mathrm{RF}, \mathrm{Im}\left(e_{z+1}^{n_t}\right)\right), \tag{12}$$

where $(X_{z+1}, Y_{z+1})$ represents the coordinate of $c_{z+1}$ ($z = 2, 3, \ldots, K-1$), $(X_z, Y_z)$ represents the coordinate of $c_z$, $\mathrm{Re}\left(e_{z+1}^{n_t}\right)$ and $\mathrm{Im}\left(e_{z+1}^{n_t}\right)$ represent the real and imaginary parts of $e_{z+1}^{n_t}$, and RF satisfies

$$\mathrm{Re}\left(e_{z+1}^{n_t}\right) + \mathrm{RF} > 0, \tag{13}$$

where RF guarantees that $c_{z+1}$ is positioned to the right of $c_z$. For a receiver with perfect channel state information (CSI), the channel characteristic $\mathbf{h}_j^{n_r, n_t}$ is calculated instantaneously in real-time to evaluate the characteristics of the channel. The module matplotlib.colors and the colormap class in matplotlib allow for mapping floating-point numbers in the range of 0 to 1 to color values. Leveraging this capability, we can define the color value for the $c_k$ ($k = 1, 2, \ldots, K$). The floating-point number corresponding to the color value of the $c_k$ is set as follows:

$$\sum_{n_r=1}^{Nr} \frac{sig\left(\left|h_{j,k}^{n_r, n_t}\right|\right)}{N_r}, \tag{14}$$

where $\left|h_{j,k}^{n_r, n_t}\right|$ represents the magnitude of $h_{j,k}^{n_r, n_t}$, and $sig(\cdot)$ refers to the sigmoid activation function. By not displaying the coordinate system and sequentially connecting $c_1, c_2, \ldots, c_K$, with the connecting lines during this process set to black, we obtain a $K$-point polyline graph with trend features, as shown in Fig. 3. It is worth noting that, during the process of handling the output of $K$-point polyline graph, we have made efforts to retain only the relevant portion of $K$-point polyline graph, thereby removing any excess blank areas surrounding $K$-point polyline graph. A $K$-point polyline graph with excessively big size can result in increased computational complexity for LG-ESDS, whereas a $K$-point polyline graph with excessively small size may distort the image. Therefore, the output format of the $K$-point polyline graph is appropriately set as 3 * 32 * 32 by the figsize function [16], where "3" refers to the number of color channels (i.e., red, green, and blue), and "32 * 32" specifies the size of the image in terms of width and height in pixels.

The above represents the mapping process of a certain $K$-point polyline graph. Considering $J$ users, each with $M$ possible transmission symbols, there are a total of $M^J$ distinct types of K-point polyline graphs, corresponding to the $M^J$ types of transmission symbol combinations (TSCs).

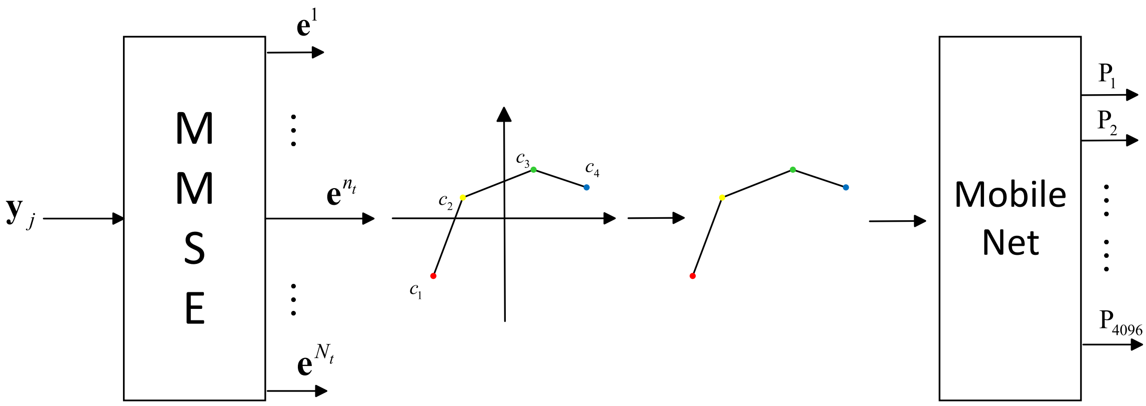


**Fig. 3** Architecture of our proposed LG-ESDS with $J = 6$, $K = 4$, and $M = 4$.

The coordinate point relay can generate various types of $K$-point polyline graphs, whose feature values include crucial information required for decoding, such as the amplitude and phase of the estimated signals, as well as the channel characteristics they have encountered. Additionally, since the coordinate of $c_{k+1}$ in the $K$-point polyline graph are derived from $c_k$, each type of $K$-point polyline graph exhibits distinct trend features. RF ensures that the Euclidean distance between the mapped coordinate points in the $K$-point polyline graph is sufficiently large. This property is beneficial for GNNs to differentiate between different types of $K$-point polyline graphs.

### 3.2.3 Full-Category Training

In the MIMO-SCMA system, the overlapping codeword corresponding to the TSC transmitted by antenna $n_t$ is mapped as a $K$-point polyline graph after MMSE detection and coordinate point relay. Based on the one-to-one correspondence between the types of TSCs and $K$-point polyline graphs, we can obtain the corresponding type of $K$-point polyline graph, by controlling the type of TSC transmitted by antenna $n_t$. The TSC corresponding to the $K$-point polyline graph is treated as a $J$-bit $M$-ary number, which equals a decimal value. And the decimal value is defined as the category of the $K$-point polyline graph. This can be expressed as follow

$$l = \sum_{j=1}^{J} m_j M^{J-j}, \tag{15}$$

where $l$ is the category of the $K$-point polyline graph, $m_j$ ($m = 0, 1, \ldots, M-1$) is the user $j$'s transmission symbol.

Unlike [12] which generates simulated data of TSCs with random categories for training DNNs, our proposed LG-ESDS adopts a full-category training approach. Specifically, an equal proportion of each type of TSCs' simulated data is generated at the transmitter of the MIMO-SCMA system, allowing GNNs to learn the features of all types of $K$-point polyline graphs in a systematic manner. During each communication process of generating the $K$-point polyline graph, we consider the dynamic changes of $\mathbf{h}_j^{n_r,n_t}$ and perform real-time calculations accordingly to determine the color value of $c_k$.

In order to find the optimal $E_b/N_0$ value for training, we test the following scenarios in this paper.

- S: train the model using a $E_b/N_0$ value of 6 dB
- M: train the model using a $E_b/N_0$ value of 8 dB
- B: train the model using a $E_b/N_0$ value of 10 dB

To classify a $K$-point polyline graph and predict the $\log_2(M)$ data bits for user $j$, we train the GNNs' parameters by minimizing the following loss function:

$$L(\mathbf{p}, \mathbf{b}) = -\sum_{i=1}^{M^J} b_i \log(p_i), \tag{16}$$

where function $L(\cdot)$ is the well-known cross-entropy loss, $\mathbf{p} = [p_1, \ldots, p_{M^J}]^T$ is the output of GNNs' softmax layer, and $\mathbf{b}$ represents the corresponding one-hot label of the index allocated by the class_to_idx function [16].

After successfully categorizing the $K$-point polyline graph, user $j$ may determine the associated TSC since there is a one-to-one correlation between the $K$-point polyline graph and the TSC in categories. User $j$ is able to recreate his own original $\log_2(M)$ binary bits $\mathbf{b}_j^{n_t}$ after masking the transmission symbols of other users in the known TSC.

### 3.2.4 Model Configuration

In this letter, we consider a basic downlink MIMO-SCMA system model with $J = 6$, $K = 4$, and $M = 4$. Regarding the number of antennas, we also consider both cases of $n_t = n_r = 2$ and $n_t = n_r = 4$ simultaneously. The components of the channel gain vector $\mathbf{h}_j^{n_r,n_t}$ are modeled as independently and identically distributed (i.i.d.) complex Gaussian random variables with zero mean and unit variance. Each method in this letter is using the same codebook provided by [17]. The whole $K$-point polyline graph set has 2,048,000 samples. The batch size is set to 64, and the number of iterations is set to 400. In order to minimize the loss function in Eqs. (16), we adopt stochastic gradient descent (SGD) optimizer [18], in which the learning rate is set as 0.002 and the momentum

**Table 1** Structure of modified version of the MobileNet model.

| Type / Stride | Filter Shape | Input Size |
|---|---|---|
| Conv / s2 | 3×3×3×8 | 32×32×3 |
| Conv dw / s1 | 3×3×8 dw | 16×16×8 |
| Conv / s1 | 1×1×8×8 | 16×16×8 |
| Conv dw / s2 | 3×3×8 dw | 16×16×8 |
| Conv / s1 | 1×1×8×8 | 8×8×8 |
| Conv dw / s1 | 3×3×8 dw | 8×8×8 |
| Conv / s1 | 1×1×8×16 | 8×8×8 |
| Conv dw / s1 | 3×3×16 dw | 8×8×16 |
| Conv / s1 | 1×1×16×16 | 8×8×16 |
| Conv dw / s1 | 3×3×16 dw | 8×8×16 |
| Conv / s1 | 1×1×16×16 | 8×8×16 |
| Conv dw / s1 | 3×3×16 dw | 8×8×16 |
| Conv / s1 | 1×1×16×32 | 8×8×16 |
| Conv dw / s2 | 3×3×32 dw | 8×8×32 |
| Conv / s1 | 1×1×32×32 | 4×4×32 |
| Avg Pool / s1 | Pool 4×4 | 4×4×32 |
| FC / s1 | 32×4096 | 1×1×32 |
| Softmax / s1 | Classifier | 1×1×4096 |

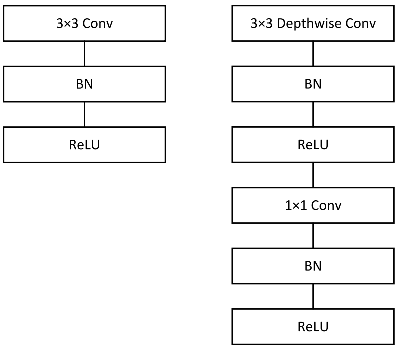


**Fig. 4** Left: standard convolutional layer with batchnorm and ReLU. Right: depthwise Separable convolutions with depthwise and pointwise layers followed by batchnorm and ReLU.

is set as 0.9. The colormap utilized in the experiment is jet [16], and the value of RF is determined in Sect. 4.2.

A modified MobileNet [15] model has been adopted as the GNN, and its architecture is shown in Table 1. In the structure of the GNN, apart from the first layer of convolutional layers which is a full convolutional, all other convolutional layers are depthwise separable convolutional layers. The distinction between depthwise separable convolutional layers and standard convolutional layers is illustrated in Fig. 4.

## 4. Analysis of Simulation Results

In Sect. 4.1, we identify the optimal $E_b/N_0$ value for LG-ESDS training. In Sect. 4.2, we determine the optimum value of RF for generating the $K$-point polyline graphs. In Sect. 4.3, we compare the performance of our LG-ESDS with the conventional separated detection algorithm and the joint detection scheme on BER over different MIMO channel configurations. In Sect. 4.4, We evaluate the computational complexity of our LG-ESDS, along with the conventional separated detection algorithm and the joint detection schemes over the 2×2 MIMO channel.

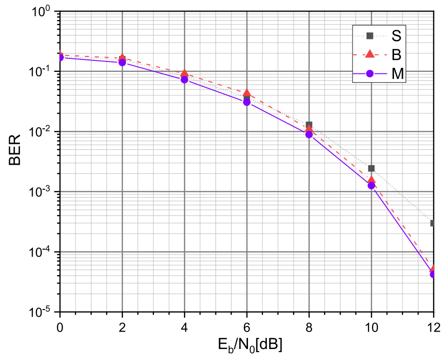


**Fig. 5** Find the optimal $E_b/N_0$ value for the training of LG-ESDS over the 2×2 MIMO channel.

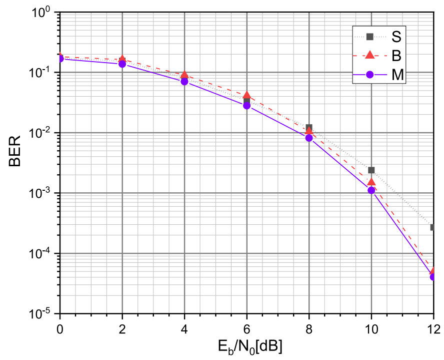


**Fig. 6** Find the optimal $E_b/N_0$ value for the training of LG-ESDS over the 4×4 MIMO channel.

### 4.1 Choice of the Optimal $E_b/N_0$ Value

Figure 5 and Fig. 6 show the BER performance of the LG-ESDS over the 2×2 and 4×4 MIMO channels respectively, after it has been trained using each of the aforementioned scenarios. During the experiment, the value of RF is temporarily set as 5. The simulation results demonstrate that, in comparison to the alternative scenarios, M emerges as the optimal training strategy. Therefore the $E_b/N_0$ value for training is set as 8 dB in the rest of this work.

### 4.2 Determination of the Optimum Value of RF

We run simulations for each of the following three scenarios to determine the optimum value of RF, over the 2×2 and 4×4 MIMO channels respectively.

- RFS: set the value of RF as 4
- RFM: set the value of RF as 5
- RFB: set the value of RF as 6

As shown in Fig. 7 and Fig. 8, the simulation achieves the greatest outcomes in scenario RFM. Therefore, in LG-ESDS, the value of RF is set as 5.

### 4.3 BER Comparison

Figure 9 and Fig. 10 compare the BER performance of our

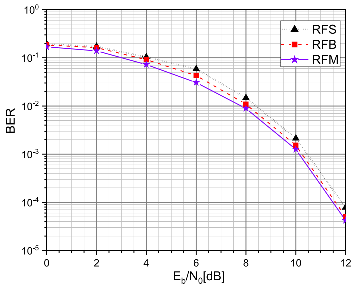


**Fig. 7** Determine the optimum value of RF over the 2×2 MIMO channel.

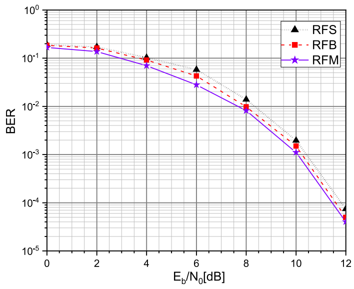


**Fig. 8** Determine the optimum value of RF over the 4×4 MIMO channel.

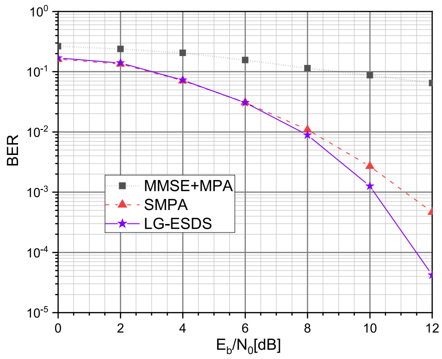


**Fig. 9** BER comparison of MMSE+MPA, SMPA and LG-ESDS over the 2×2 MIMO channel.

LG-ESDS with the conventional separated detection algorithm (MMSE+MPA) and the joint detection scheme (Serial Schedule strategy based MPA (SMPA) [10]) over the 2×2 and 4×4 MIMO channels respectively. Our LG-ESDS consistently outperforms MMSE+MPA (8 iterations) across different $E_b/N_0$ values, and also achieves lower BER than SMPA (5 iterations) at high $E_b/N_0$ values. It is noteworthy that when the value of $E_b/N_0$ exceeds 6 dB, as $E_b/N_0$ increases, the BER performance of LG-ESDS compared to SMPA becomes more significant. This can be explained that compared to other MIMO-SCMA decoding strategies, our LG-ESDS does not require continuous message exchange between R nodes and U nodes, it can directly utilize the effective information of the estimated signals. Furthermore, our LG-ESDS exploits more features (the trend features of the $K$-point polyline graphs), which is beneficial for image classification.

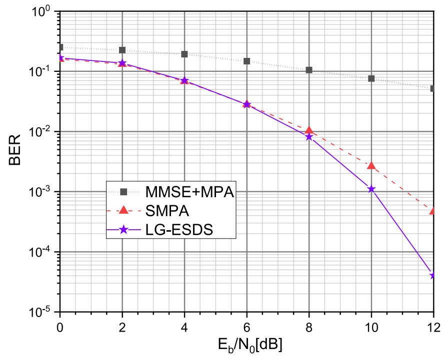


**Fig. 10** BER comparison of MMSE+MPA, SMPA and LG-ESDS over the 4×4 MIMO channel.

### 4.4 Complexity Analysis

The computational cost of conventional convolution can be expressed as follows:

$$K_s \cdot K_s \cdot N_{in} \cdot N_{out} \cdot D \cdot D, \tag{17}$$

where $K_s \times K_s$ is the kernel size, $N_{in}$ denotes the number of input channels, $N_{out}$ represents the number of output channels, and $D \times D$ is the output feature map size. The computational cost of depthwise separable convolution can be expressed as follows:

$$K_s \cdot K_s \cdot N_{in} \cdot D \times D + N_{in} \cdot N_{out} \cdot D \times D \tag{18}$$

And the computational cost of fully connected layer can be expressed as follows:

$$N_n \cdot N_c, \tag{19}$$

where $N_n$ is the number of neurons in the fully connected layer, and $N_c$ denotes the number of neurons in the output layer.

The computational complexity of the MMSE detection and the generation of the $K$-point polyline graph can be considered negligible compared to the computational complexity of the convolutional computation. Based on Eqs. (17), Eqs. (18), and Eqs. (19), we calculate the computational complexity of our proposed LG-ESDS and compare it with MMSE+MPA (8 iterations), SMPA (5 iterations), and improved maximum distance MPA (IMDMPA (3 iterations)) [11], as illustrated in Fig. 11. Our LG-ESDS exhibits lower computational complexity compared to the other three decoding strategies. It should be mentioned that in order to reach performance convergence, different decoding strategies may require varying numbers of iterations. In order to ensure fairness in our comparison of computational complexity, we fix the number of iterations for each strategy to be the bare minimum needed to achieve performance convergence. Although our adopted GNNs in comparison to the original version of MobileNet has undergone significant simplifications, the extreme similarity in the distribution of the same type of $K$-point polyline graph features ensures that

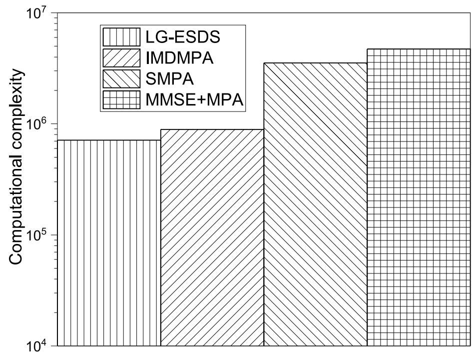


**Fig. 11** Computational complexity comparison of MMSE+MPA, SMPA, IMDMPA and LG-ESDS over the 2×2 MIMO channel.

our LG-ESDS can achieve the decoding performance illustrated in Sect. 4.3. It is worth mentioning that as the number of antennas increases in the MIMO-SCMA system, the computational complexity of various decoding algorithms also significantly increases. In such cases, our LG-ESDS exhibits even more pronounced advantages over other decoding algorithms in terms of computational complexity.

## 5. Conclusion

We have proposed a lightweight GNNs based enhanced separated detection scheme to accomplish the multi-user detection tasks at the receiver of the downlink MIMO-SCMA systems. We have raised the concepts of coordinate point relay and full-category training, which replacing the MPA in SCMA decoding with GNNs based image classification technology and offering a more methodical and rigorous experimental approach. Our LG-ESDS achieves a balance between computational complexity and BER performance, outperforming other decoding algorithms.

## Acknowledgments

This work was partially supported by the Natural Science Foundation of Xinjiang Uygur Autonomous Region under Grant 2022D01C426 and supported by the Graduate Research Innovation Project of Xinjiang Uygur Autonomous Region under Grant XJ2023G100.

### References

[1] Y.-P.E. Wang, X. Lin, A. Adhikary, A. Grovlen, Y. Sui, Y. Blankenship, J. Bergman, and H.S. Razaghi, "A primer on 3GPP narrowband Internet of Things," IEEE Commun. Mag., vol.55, no.3, pp.117–123, March 2017.

[2] D.W.K. Ng and R. Schober, "Resource allocation and scheduling in multicell OFDMA systems with decode-and-forward relaying," IEEE Trans. Wireless Commun., vol.10, no.7, pp.2246–2258, July 2011.

[3] L. Dai, B. Wang, Y. Yuan, S. Han, I. Chih-lin, and Z. Wang, "Nonorthogonal multiple access for 5G: Solutions, challenges, opportunities, and future research trends," IEEE Commun. Mag., vol.53, no.9, pp.74–81, Sept. 2015.

[4] H. Nikopour and H. Baligh, "Sparse code multiple access," Proc. IEEE 24th Annu. Int. Symp. Pers. Indoor Mobile Radio Commun., London, U.K., pp.332–336, 2013.

[5] F. Rusek, D. Persson, B.K. Lau, E.G. Larsson, T.L. Marzetta, and F. Tufvesson, "Scaling up MIMO: Opportunities and challenges with very large arrays," IEEE Signal Process. Mag., vol.30, no.1, pp.40–60, Jan. 2013.

[6] M. Moltafet, S. Parsaeefard, M.R. Javan, and N. Mokari, "Robust radio resource allocation in MISO-SCMA assisted C-RAN in 5G networks," IEEE Trans. Veh. Technol., vol.68, no.6, pp.5758–5768, June 2019.

[7] S. Qian, W. Ge, Y. Zhang, and P. Zhang, "A large-scale SCMA codebook optimization and codeword allocation method," IEICE Trans. Commun., vol.E105-B, no.7, pp.788–796, July 2022.

[8] S.S. Yang and L. Hanzo, "Fifty years of MIMO detection: The road to large-scale MIMOs," IEEE Commun. Surveys Tuts., vol.17, no.4, pp.1941–1988, 4th Quart., 2015.

[9] L. Yang, Y. Liu, and Y. Siu, "Low complexity message passing algorithm for SCMA system," IEEE Commun. Lett., vol.20, no.12, pp.2466–2469, 2016.

[10] Y. Du, B. Dong, Z. Chen, P. Gao, and J. Fang, "Joint sparse graph-detector design for downlink MIMO-SCMA systems," IEEE Wireless Commun. Lett., vol.6, no.1, pp.14–17, Feb. 2017.

[11] H. Cheng, C. Zhang, Y. Huang, and L. Yang, "Efficient message passing receivers for downlink MIMO-SCMA systems," IEEE Trans. Veh. Technol., vol.71, no.5, pp.5073–5086, May 2022.

[12] M. Kim, N.-I. Kim, W. Lee, and D.-H. Cho, "Deep learning-aided SCMA," IEEE Commun. Lett., vol.22, no.4, pp.720–723, 2018.

[13] Q. Yuan, Z. Wang, D. Li, Q. Guo, and W. Xiang, "Sparse code multiple access scheme based on variational learning," IEICE Trans. Commun.,, vol.70, no.12, pp.7989–8002, Dec. 2022.

[14] S. Dörner, S. Cammerer, J. Hoydis, and S. ten Brink, "Deep learning based communication over the air," IEEE J. Sel. Topics Signal Process., vol.12, no.1, pp.132–143, Feb. 2017.

[15] A.G. Howard, M. Zhu, B. Chen, D. Kalenichenko, W.J. Wang, T. Weyand, M. Andreetto, and H. Adam, "MobileNets: Efficient convolutional neural networks for mobile vision applications," 2017, [online] Available: https://arxiv.org/abs/1704.04861

[16] A. Paszke, et al., "PyTorch: An imperative style, high-performance deep learning library," Proc. Adv. Neural Inf. Process. Syst., 2019, pp.8026–8037.

[17] Altera Innovate Asia FPGA Design Contest. (2015) 5G Algorithm Innovation Competition.

[18] S. Ruder, "An overview of gradient descent optimization algorithms," arXiv:1609.04747, 2016.

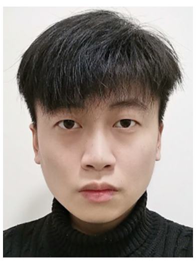

**Zikang Chen** received the B.S. degree in Communication Engineering at China University of Geosciences (Wuhan) in 2020. At present, he majors in Information and Communication Engineering at Xinjiang University for M.S. degree.

**Wenping Ge** received the Ph.D. degree in Electromagnetic and Microwave Technology at Shanghai Jiaotong University in 2003. Her research interests include wireless communication, optical crystal fiber, and optoelectronic materials. She is full professor in College of Information Science and Technology, Xinjiang University. Her current research interests include sparse code multiple access and codebook design in wireless communications.

**Henghai Fei** received the B.S. degree in Communication Engineering at Jilin University in 2020. At present, he majors in Information and Communication Engineering at Xinjiang University for M.S. degree.

**Haipeng Zhao** received the B.S. degree in Communication Engineering at Jinan University in 2020. At present, he majors in Electronic and Communication Engineering at Xinjiang University for M.E. degree.

**Bowen Li** received the B.S. degree in Communication Engineering at Wuhan Textile University in 2021. At present, he majors in Electronic and Communication Engineering at Xinjiang University for M.E. degree.

PAPER

# SimpleViTFi: A Lightweight Vision Transformer Model for Wi-Fi-Based Person Identification

**Jichen BIAN**[†,††], ***Student Member***, **Min ZHENG**[†], **Hong LIU**[†], **Jiahui MAO**[†,††], **Hui LI**[†], ***and*** **Chong TAN**[†a)], ***Nonmembers***

**SUMMARY** Wi-Fi-based person identification (PI) tasks are performed by analyzing the fluctuating characteristics of the Channel State Information (CSI) data to determine whether the person's identity is legitimate. This technology can be used for intrusion detection and keyless access to restricted areas. However, the related research rarely considers the restricted computing resources and the complexity of real-world environments, resulting in lacking practicality in some scenarios, such as intrusion detection tasks in remote substations without public network coverage. In this paper, we propose a novel neural network model named SimpleViTFi, a lightweight classification model based on Vision Transformer (ViT), which adds a downsampling mechanism, a distinctive patch embedding method and learnable positional embedding to the cropped ViT architecture. We employ the latest IEEE 802.11ac 80MHz CSI dataset provided by [1]. The CSI matrix is abstracted into a special "image" after pre-processing and fed into the trained SimpleViTFi for classification. The experimental results demonstrate that the proposed SimpleViTFi has lower computational resource overhead and better accuracy than traditional classification models, reflecting the robustness on LOS or NLOS CSI data generated by different Tx-Rx devices and acquired by different monitors.

***key words:*** *Wi-Fi sensing, CSI, person identification, lightweight model, vision transformer*

## 1. Introduction

With the continuous evolution of Wi-Fi protocols [2], [3] and the exponential growth of Wi-Fi devices, people are no longer solely focused on using Wi-Fi for Internet access. Instead, there is an increasing demand for higher bandwidth, more reliable connections, and improved service quality to accommodate applications such as high-immersive gaming and remote healthcare [4]. This shift has led to the emergence of a more versatile and robust wireless communication infrastructure that not only provides seamless connectivity but also enables novel sensing and interaction capabilities. It is widely recognized that Wi-Fi sensing plays a crucial role in various tasks, including indoor activity recognition, object sensing, and localization [5], [6]. By leveraging the fine-grained channel variations captured in Wi-Fi CSI, researchers can extract meaningful features that correlate with real-world positions, actions, and states [7]. This capability paves the way for an array of novel prospects in the domain of pervasive and context-aware computing applications, including intelligent residential environments, assisted living arrangements, and advanced security systems [5], [8]. However, there exist challenges in achieving efficient Wi-Fi sensing in resource-constrained environments. For instance, remote substations in underdeveloped areas need to deploy the intrusion detection system due to their critical energy supply role and potential security risks. Conventional camera detection is difficult to illuminate at night and to guarantee dead-end coverage, not to mention the large demand for computing resources. Meanwhile, such substations often lack public network coverage because of the remote location, making it hard to access cloud servers for the deployment of highly resource-intensive detection applications [9], [10]. In such scenarios, the lightweight and effective Wi-Fi-based PI method is considered as a reliable alternative, which can operate with local, limited resources [6]. We aim to advance the state-of-the-art of Wi-Fi sensing at the edge and contribute to its broader applicability in challenging environments. This will ultimately enable the deployment of Wi-Fi sensing technologies in a wider range of real-world scenarios, thus improving the efficiency and safety of critical infrastructure management [5].

At present, a multitude of research employs Wi-Fi sensing technology for various tasks. [11] introduces Wisleep, a system that infers sleep duration using passively sensed smartphone network connections from Wi-Fi infrastructure, achieving comparable accuracy to client-side methods. An unavoidable limitation, though, is a reliance on users carrying devices, while current research trends are shifting towards device-free detection methods for greater convenience and user comfort. [12] proposes Temporal Unet, a deep convolutional neural network for sample-level action recognition in the Wi-Fi sensing domain, enabling precise action localization and real-time recognition. Nevertheless, this paper does not address potential issues related to computational complexity and generalizability across diverse environments. [13] presents FewSense, a few-shot learning-based Wi-Fi sensing system capable of recognizing novel classes in unseen domains using limited samples, achieving high accuracy on three public datasets (SignFi, Widar, and Wiar) and improving performance through collaborative sensing while limiting in the large model size, which may render it unsuitable for computationally constrained environments despite its effectiveness in cross-domain scenarios.

Manuscript received June 15, 2023.
Manuscript revised September 22, 2023.
Manuscript publicized January 30, 2024.
[†]The authors are with Shanghai Institute of Microsystem and Information Technology, Chinese Academy of Sciences, Shanghai, 200050, China.
[††]The authors are with University of Chinese Academy of Sciences, Beijing, 101408, China.
a) E-mail: chong.tan@mail.sim.ac.cn
DOI: 10.23919/transcom.2023EBP3102

Despite a great deal of research being conducted, there is still a lack of studies on Wi-Fi sensing focusing on resource-constrained environments. In this paper, we propose a novel neural network model named SimpleViTFi based on ViT. This model performs well on person identification tasks using CSI data generated from Wi-Fi devices. Our developments are inspired by works in [8], [14]. The developments can be concretely described as follows:

(1) Drawing inspiration from the ViT model in the field of Computer Vision (CV), we propose a lightweight ViT model with distinctive patch segmentation, downsampling operation, reduced number of layers, and efficient feature extraction capabilities, termed as SimpleViTFi, specifically designed for PI tasks in the Wi-Fi sensing domain under resource-constrained scenarios.

(2) We conduct a comparative analysis of the impact of two types of position encoding methods - the sin-cos method and learnable embedding - on PI. The results show that the learnable embedding method yields superior performance, and we delve into a discussion attempting to analyze the possible explanations for this outcome.

(3) We benchmark SimpleViTFi against several popular models, including LeNet, ResNet18, and GRU. SimpleViTFi significantly outperforms these models on Wi-Fi-based PI tasks. Furthermore, we introduce an incremental learning approach to further enhance the performance and efficiency of SimpleViTFi, which requires a little extra time and data to achieve robust performance across different CSI datasets generated by various Wi-Fi devices.

The structure of this paper unfolds as follows: Section 2 delves into a comprehensive discussion on related works. Section 3 provides the detail of the proposed SimpleViTFi. Section 4 shows the experimental setup and comparisons of the results with existing works. Section 5 concludes this paper and provides recommendations for some future research topics.

## 2. Related Works

In this section, we survey the existing literature on Wi-Fi sensing using CSI data. Research work in the Wi-Fi sensing field bifurcates into two main directions: fundamental model research and application-oriented research. From a methodological perspective, there exists a gradual shift in focus from traditional statistical modeling methods to artificial intelligence (AI) methods.

In terms of fundamental model research, Yang et al. [7] propose an automatic Wi-Fi human sensing learning framework called AutoFi, which can achieve automatic Wi-Fi human sensing with minimal manual annotation. AutoFi can train a robust model from low-quality CSI samples, making it easier to use Wi-Fi sensing technology in new environments. The paper also analyzes the main gaps between existing learning-based methods and practical Wi-Fi sensing, proposing a novel self-supervised learning framework and a new geometric structure loss function to enhance the model's transferability. Extensive experiments are conducted on public datasets and real-world scenarios, demonstrating the high accuracy and robustness of the AutoFi method in automatic Wi-Fi human sensing. In another study, Hernandez and Bulut [15] present WiFederated, a federated learning approach for training machine learning models for Wi-Fi sensing tasks. This method allows for parallel training at the edge, enabling devices to collaboratively learn and share location-independent physical behavior features. The authors demonstrate that their method diminishes the necessity for extensive data collection at each new location, offering a solution that is more accurate and time-efficient compared to both transfer learning and adversarial learning solutions. Liu et al. [16] propose a deep learning-based Wi-Fi sensing approach using a CNN-BiLSTM architecture to identify vigorous activities. This architecture can simultaneously extract sufficient spatiotemporal features of action data and establish the mapping relationship between actions and CSI streams, thereby improving activity recognition accuracy.

In terms of application-oriented research, several mature systems have been developed, showcasing the unique charm of Wi-Fi sensing in various fields. Tong et al. [17] propose FreeSense, a combination of Principal Component Analysis (PCA), Discrete Wavelet Transform (DWT) and Dynamic Time Warping (DTW) techniques, using for CSI waveform-based human identification. The identification accuracy of FreeSense ranges from 94.5% to 88.9% when the number of users changes from 2 to 6. Lin et al. [18] represent WiTL, a contactless authentication system based on Wi-Fi CSI. It is devised using a transfer learning technology, in combination with ResNet and the adversarial network, to extract activity features and learn environment-independent representations. WiTL achieves a great accuracy over 93% and 97% in multi-scenes and multi-activities identity recognition, respectively.

In spite of a few existing studies of Wi-Fi-based PI tasks, they rarely consider the feasibility in resource-constrained environments. Therefore, we would like to combine the latest research based on Wi-Fi sensing and AI methods to make innovations in resource-constrained PI tasks.

## 3. Methodology

### 3.1 Channel State Information

Channel State Information (CSI) [19] is a critical component in Wi-Fi sensing systems. It represents the combined effects of the wireless channel's propagation properties, including path loss, shadowing, and multipath fading, which are affected by the environment and the presence of objects or people. CSI can be modeled as channel impulse response (CIR) in the frequency domain as

$$h(\tau) = \sum_{l=1}^{L} \alpha_l e^{j\phi_l} \delta(\tau - \tau_l), \tag{1}$$

where $\alpha_l$ and $\phi_l$ respectively represent the amplitude and phase of the $l$_th multipath component, $\tau_l$ is the time delay, $L$ indicates the total number of multipath components, and $\delta(\tau)$ denotes the Dirac delta function. CSI has been widely used in Wi-Fi sensing research to exploit the rich information it contains about the surrounding environment and human activities.

CSI can be obtained from commodity Wi-Fi devices. When a transmitter transmits a signal $x$, it is received by the receiver as $y = Hx + \eta$, where $\eta$ represents environmental noise and $H$ represents the CSI complex-valued matrix. Each element in the matrix corresponds to the channel gain between a specific transmitter-receiver antenna pair in a MIMO system. The matrix's dimensions depend on the number of transmitting and receiving antennas. In addition, the CSI matrix is also influenced by the number of Orthogonal Frequency Division Multiplexing (OFDM) subcarriers. The more subcarriers, the finer the frequency resolution, which allows for a more accurate representation of the channel characteristics [20].

The CSI matrix $H$ for a system with $N$ transmitting antennas and $M$ receiving antennas can be represented as:

$$\mathrm{CSI}_{N\times M} = \begin{bmatrix} h_{11} & h_{12} & \dots & h_{1M} \\ h_{21} & h_{22} & \dots & h_{2M} \\ \vdots & \vdots & \ddots & \vdots \\ h_{N1} & h_{N2} & \dots & h_{NM} \end{bmatrix} \tag{2}$$

In this representation, $h_{ij}$ is a complex vector that represents the channel gain between the $i$-th transmitting antenna and the $j$-th receiving antenna. The amplitude and phase of each $h_{ij}$ can be calculated as follows:

$$\mathrm{Amp}(h_{ij}) = |h_{ij}| = \sqrt{\mathrm{Re}(h_{ij})^2 + \mathrm{Im}(h_{ij})^2} \tag{3}$$

$$\mathrm{Pha}(h_{ij}) = \angle h_{ij} = \arctan\left(\frac{\mathrm{Im}(h_{ij})}{\mathrm{Re}(h_{ij})}\right) \tag{4}$$

### 3.2 Vision Transformer

Vision Transformer (ViT) [21], [22] has emerged as a powerful and flexible approach for solving various CV tasks, inspired by the success of Transformers in natural language processing (NLP). ViT is a type of neural network architecture that can process images by dividing them into non-overlapping patches and treating these patches as a sequence of tokens, similar to how Transformers process texts.

The core component of ViT is the self-attention mechanism, which allows the model to learn long-range dependencies between different parts of the image. This mechanism enables ViT to capture both local and global contextual information and adaptively focus on relevant regions in the image.

ViT has demonstrated state-of-the-art performance on a wide range of CV tasks, such as image classification, object detection, and semantic segmentation [23], outperforming traditional convolutional neural networks (CNNs). The flexibility and expressiveness of ViT make them a promising approach for various CV tasks, including those that require fine-grained visual understanding and adaptability to different input modalities [24].

In this paper, we treat the CSI matrix as a multi-channel "image" and attempt to address the CSI-based PI tasks with ViT. From our perspective, CSI images differ from traditional RGB images in two aspects:

(1) The weights in CSI images are evenly distributed across all pixels, unlike conventional images that typically have a focal point and a background. The global receptive field of ViT can better capture the features of CSI images due to this uniform distribution.
(2) CSI images have a temporal dimension, necessitating a focus on the relationships and changes along this dimension. ViT, with its unique sensitivity to positional relationships, is well-suited to this task.

Therefore, this paper aims to explore the potential of ViT in the realm of CSI-based classification, hoping to uncover the unique capabilities of this technology in handling such tasks.

### 3.3 SimpleViTFi

As shown in Fig. 1, we propose SimpleViTFi, which is designed for processing CSI images with a focus on efficient feature extraction and classification. SimpleViTFi is inspired by the ViT and incorporates several key components with data flow as shown by the bold red arrows. SimpleViTFi comprises the following main components:

**Patch Embedding**: The input CSI matrix $\mathbf{X} \in \mathbb{R}^{B\times A\times S\times T}$ is first downsampled and divided into non-overlapping patches along the temporal dimension, where the dimensions represent the number of antennas($A$), subcarriers($S$), and the time sequence($T$) respectively. Then the patches are linearly embedded into a higher-dimensional feature space. A Layer Normalization operation is applied to the embedded patches. Unlike traditional image patch segmentation methods, we do not partition the data along the subcarrier dimension, as we prefer the model to focus on the temporal dimension.

**Position Encoding**: Learnable positional embeddings $\mathbf{P} \in \mathbb{R}^{S\times T}$ are added to the patch embeddings to capture the spatial relationships between the patches in SimpleViTFi. There are two main types of positional embeddings:

(1) Fixed Positional Embbdings follow the original method in [25], which are initialized with a sinusoidal function.
(2) Learnable Positional Embeddings are initialized randomly and then updated through backpropagation during the training process.

The CSI dataset involves complicated spatial and temporal relationships across different antennas and subcarriers. This multi-dimensional complexity could pose challenges to traditional sinusoidal position encodings such as the sin-cos method used in the Transformer model, which provides a fixed encoding based on the position of data points in the sequence. In contrast, learnable positional embeddings, added to the patch embeddings to capture the spatial relationships between time sequences, offer a more flexible approach. By

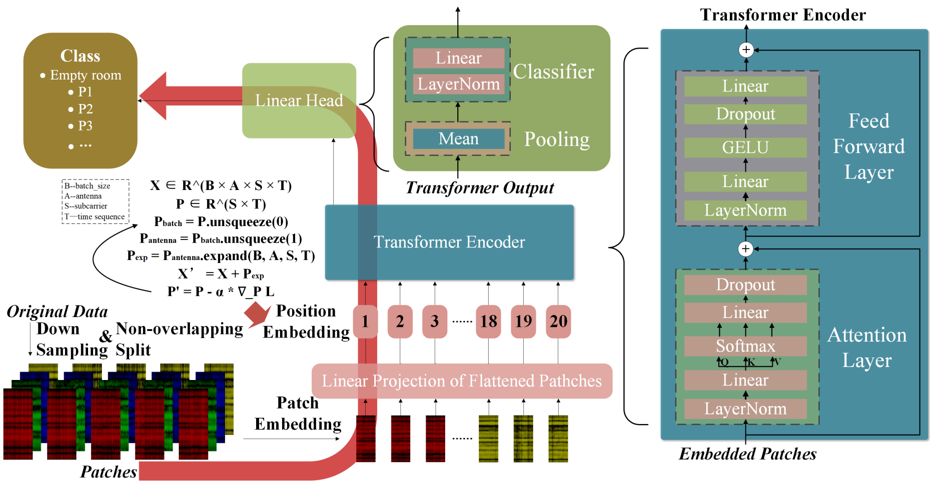


**Fig. 1** SimpleViTFi model.

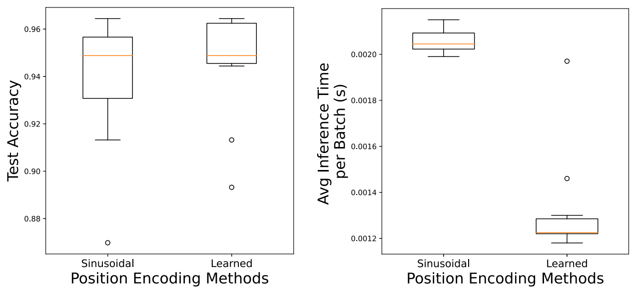


(a) Test Accuracy with Two Position Methods

(b) Inference Time with Two Position Methods

**Fig. 2** Test accuracy and inference time of two position methods.

allowing the model to learn the position embeddings from the data itself, it could enable the discovery of more intricate or subtle patterns in the sequence order, thereby improving its ability to identify individuals.

We compare two methods mentioned above: the sin-cos method and learnable embedding. Figure 2(a) shows that the learnable embedding achieves a more consistent high rate of accuracy within 20 replicate experiments, as it enables the model to adapt to the specific patterns present in the CSI data. Although using learnable embedding increases the number of parameters and requires additional optimization during training, it results in a shorter inference time compared to the other as shown in Fig. 2(b). This is attributable to the learnable embedding being computed in parallel, whereas the sin-cos method requires sequential computation. The combined embeddings can be represented as $\mathbf{X}' = \mathbf{X} + \mathbf{P}exp$, where $\mathbf{P}exp \in \mathbb{R}^{B \times A \times S \times T}$ is the expanded version of $\mathbf{P}$.

**Transformer Encoder**: The combined patch and positional embeddings are fed into a Transformer encoder, which consists of multiple layers of multi-head self-attention and feedforward neural networks. In the experiments that follow, we employ 2 layers of self-attention and feedforward networks.

**Pooling**: Following the Transformer encoder, a global average pooling operation is performed to aggregate the features across the sequence dimension. This operation reduces the dimensionality of the output and prepares it for the classification head. The pooled features can be represented as $\mathbf{Z} = \text{mean}(\mathbf{X}', 1)$.

**Classifier Head**: The pooled features $\mathbf{Z}$ are then passed through a LayerNormalization layer, which can be represented as:

$$\mathbf{Z}norm = \frac{\mathbf{Z} - \text{E}[\mathbf{Z}]}{\sqrt{\text{Var}[\mathbf{Z}] + \epsilon}}, \tag{5}$$

where E[.] is the expectation operation, Var[.] is the variance operation, and $\epsilon$ is a small constant for numerical stability. The normalized features $\mathbf{Z}norm$ are subsequently processed by a Linear layer that maps the features to the desired number of output classes. This can be represented as:

$$\mathbf{Y} = \mathbf{W}\left(\frac{\mathbf{Z} - \text{E}[\mathbf{Z}]}{\sqrt{\text{Var}[\mathbf{Z}] + \epsilon}}\right) + \mathbf{b}, \tag{6}$$

where W is the weight matrix and b is the bias vector of the Linear layer.

The SimpleViTFi architecture is designed to be lightweight and efficient while maintaining high performance on the task of processing and classifying CSI matrices. By leveraging the strengths of both Vision Transformers and learned positional embeddings, the SimpleViTFi model demonstrates the robustness and adaptability to various CSI data patterns.

## 4. Experiment

### 4.1 80 MHz CSI Dataset of IEEE 802.11ac

The datasets mentioned in [1], [14] consisting of three types of datasets applicable to activity recognition (AR), person identification (PI), and people counting (PC), are produced by the University of Padova. Our focus is on the subset dedicated to PI in this paper.

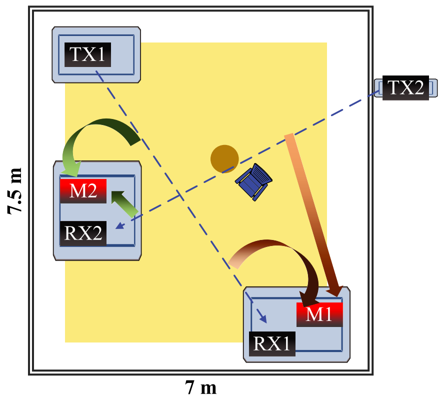


**Fig. 3** Devices and users' positions in the meetingroom.

**Table 1** Measurement conditions of the dataset.

| | **PI-1** | **PI-2** | **PI-3** | **PI-4** |
|---|---|---|---|---|
| **w×l×h** | 7m×7.5m×3.5m | | | |
| **obst.** | × | ✓ | × | ✓ |
| **devices pos.** | M1-Tx1-Rx1 | M1-Tx2-Rx2 | M2-Tx1-Rx1 | M2-Tx2-Rx2 |
| **Tx** | Netgear | Netgear | Netgear | Netgear |
| **Rx** | Netgear | TP-Link | Netgear | TP-Link |
| **furniture** | 7 desks, chairs | | | |

**Dataset Experiment Setup:**As shown in Fig. 3, the experiments are set within a meeting room. Two pairs of devices are strategically positioned. Specifically:

- Tx1 communicates with Rx1, establishing a line-of-sight (LOS) condition.
- Tx2 communicates with Rx2, resulting in a non-line-of-sight (NLOS) condition.

Additionally, two monitors, M1 and M2, are positioned to sniff and calculate the CSI data from both communication links. Consequently, each monitor stores two distinct sets of CSI data, named PI-1 – PI-4 shown in Table 1.

**CSI Collection Method:** An iPerf3 session is established between each pair of Tx and Rx, transmitting at a consistent rate of 173 packets per second. This rate corresponds to time intervals of approximately 6ms between each packet. The monitors configure the Nexmon-CSI extraction tool [26] to sniff packets continuously. The dataset involves 10 participants, each of whom moves individually and randomly within the colored areas in Fig. 3.

### 4.2 Data Preprocessing

Taking PI2_p03 as an example, this file represents the CSI data of Participant-3 created by Tx2 and Rx2, which is monitored by M1 in NLOS condition. It is a complex matrix of size $187264 \times 256$, where 256 represents the number of OFDM subcarriers under the 80MHz bandwidth, and 187264 represents the CSI indices of 46816 packets obtained separately by the four antennas. We preprocess this data file as follows:

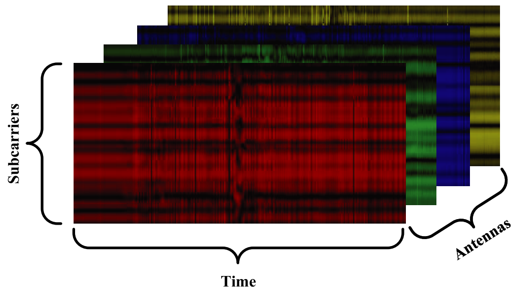


**Fig. 4** CSI amplitude matrix.

(1) Load raw data and apply a Fast Fourier Transform shift operation.
(2) Remove invalid subcarriers and zero-sum rows from the CSI matrix, retaining 242 subcarriers.
(3) Calculate the number of complete groups of 4-antenna CSI data.
(4) Due to hardware artifact, negate the data from the 64th column onwards in each group.
(5) Convert the original complex values to amplitude values by taking the modulus.
(6) Divide the matrix into submatrices of size (4, 242, 2000) using a boundary of 2000 packets, facilitating subsequent analysis.

### 4.3 Experiment Setup

To demonstrate the effectiveness of the proposed method, we use the dataset mentioned in 4.1, and implement the SimpleViTFi based on Pytorch. Then, we conduct extensive experiments to evaluate the performance of SimpleViTFi concerning classification accuracy, model parameters and inference time of PI task.

*System Design:* The edge server in resource-constrained scenarios is simulated by the PC equipped with one NVIDIA RTX 3060 GPU. To fully evaluate the performance of SimpleViTFi and the others, we attempt to set up multiple experiments comprising different data sets. Four sets of experiments are set up as shown in Table 2. Specifically:

(1) **Experiment 1**: Utilizing $\frac{2}{3}$ of the PI-1 dataset as the training set and the remaining $\frac{1}{3}$ as the test set, this experiment aims to validate the model's classification ability in handling CSI data generated from LOS condition.
(2) **Experiment 2**: By employing $\frac{2}{3}$ of the PI-4 dataset for training and the rest for testing, this experiment is designed to assess the model's classification ability with CSI data stemming from NLOS condition.
(3) **Experiment 3**: This experiment combines $\frac{2}{3}$ of the PI-1 dataset with $\frac{1}{3}$ of the PI-3 dataset to form the training set, while the remaining data serves as the test set. Both PI-1 and PI-3 generate CSI data using Tx1 and Rx1 communication link but utilize different monitors. The primary objective is to evaluate the model's robustness

**Table 2** Experiment setup.

| Experiment Index | TrainSet | TestSet | Method |
|---|---|---|---|
| 1 | PI-1(2/3) | PI-1(1/3) | LeNet<br>ResNet18<br>GRU<br>SimpleViTFi |
| 2 | PI-4(2/3) | PI-4(1/3) | |
| 3 | PI-1(2/3)<br>PI-3(1/3) | PI-1(1/3)<br>PI-3(2/3) | |
| 4 | PI-1(2/3)<br>PI-2(2/3)<br>PI-3(2/3)<br>PI-4(2/3) | PI-1(1/3)<br>PI-2(1/3)<br>PI-3(1/3)<br>PI-4(1/3) | |

**Table 3** Network design of SimpleViTFi.

| Layer_Index | Components | details |
|---|---|---|
| **input** | | CSI_amp: $4 \times 242 \times 2000$<br>( antenna pairs × subcarriers × time sequence) |
| **1** | Patch Embedding | 1) downsampling: $4 \times 121 \times 500$<br>2) 100 patches: $100 \times 4 \times 121 \times 5$ |
| **2** | Position Encoding | learnable embedding |
| **3** | Transformer Encoder | dim: 64<br>depth: 2<br>heads: 8<br>mlp_dim: 2048<br>dropout_rate: 0.3<br>learning_rate: 0.0001<br>weight_decay: 0.1<br>loss_function: CrossEntropyLoss |
| **4** | Pooling | average pooling |
| **5** | Classifier Head | $\mathbf{Y} = \mathbf{W}\left(\frac{\mathbf{Z}-\mathrm{E}[\mathbf{Z}]}{\sqrt{\mathrm{Var}[\mathbf{Z}]+\epsilon}}\right) + \mathbf{b}$ |
| **output** | | Classificaition Results |

to variations in devices' locations.

(4) **Experiment 4**: Incorporating a mixed dataset from PI-1 to PI-4, with $\frac{2}{3}$ used for training and the remainder for testing, this experiment seeks to gauge the model's resilience under the complexities of different devices and different monitors.

*Network Implementation:* The network design has been shown in Table 3. Note that Transformer Encoder is a sequence of 2 attention and feed-forward layers. The attention layer uses the scaled dot-product attention mechanism with 8 heads, and the feed-forward layer is a two-layer fully connected network with a hidden dimension of 2048 and a GELU activation function in between. The model is trained with the Adam optimizer with a learning rate of 0.0001 and a weight decay of 0.1. The loss function used is CrossEntropyLoss. The model employs an early stopping mechanism during training, which halts the training process if there is no improvement in validation loss for 8 consecutive epochs, preventing overfitting and ensuring better generalization.

*Criterion:* In our experiments, we evaluate and compare the models based on three key metrics: the number of training parameters, inference time, and identification accuracy. The identification accuracy is denoted as the ratio of true predicted samples and all testing samples.

*Baselines:* We compare our method with three traditional methods. LeNet, as one of the earliest convolutional neural networks, has made significant contributions to the field of image classification, setting the foundation for future advancements [27]. ResNet18, with its innovative residual learning framework, has further improved the performance of deep neural networks in image classification tasks, notably reducing the training error [28]. On the other hand, GRU (Gated Recurrent Unit) has shown exceptional performance in time series prediction due to its efficient gating mechanisms, which handle the vanishing gradient problem and allow for long-term dependencies [29]. In light of our approach where we interpret the Channel State Information (CSI) matrix as an image, and considering the substantial temporal correlations this 'image' embodies, we deem it appropriate to draw comparisons with the aforementioned methods.

## 4.4 Evaluation

The proposed SimpleViTFi is compared with baselines. Figure 5 illustrates the efficiency of SimpleViTFi in comparison to the others. Notably, SimpleViTFi demonstrates the shortest average inference time clocking in at 1.338 ms and requires the least number of parameters with a total of 1,079,923, which makes it consume the fewest computational complexity and memory usage with high efficiency for real-time tasks.

Following this, we examine the performance of SimpleViTFi on PI-1 (Experiment 1). In addition to the amplitude-based results shown in Fig. 6, we also incorporate phase-based results shown in Fig. 7. However, the phase-based results are not as anticipated. For all four models, the accuracy barely surpasses 25%, indicating that the models are virtually non-functional with the phase value. We believe that the potential reasons for this could be the inherent instability and sensitivity of phase to environment. Under complex multipath effects, the phase undergoes multiple cumulative changes, making it highly unstable. This heightened sensitivity can lead the model to overfit, making it challenging to capture essential features.

Returning to the amplitude-based results, as presented in Fig. 6, SimpleViTFi outperforms the others, achieving the highest accuracy on the test set. The box plot visualizes the range and distribution of accuracy scores achieved by SimpleViTFi and the others across multiple runs. The central line in the box plot represents the median accuracy, which for SimpleViTFi is an impressive 0.9566, about at least 10% higher than the others such as 0.8525 for ResNet18. The box itself spans from the first quartile (Q1) to the third quartile (Q3), representing the interquartile range (IQR). For SimpleViTFi, Q1 is 0.91037 and Q3 is 0.9566. This range captures the middle 50% of accuracy scores, providing a sense of the model's consistency. This consistency, coupled

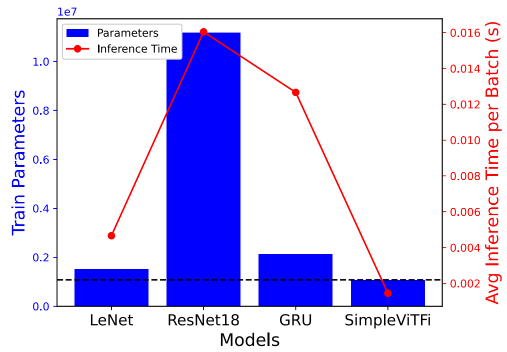


**Fig. 5** Train parameters and inference time per batch.

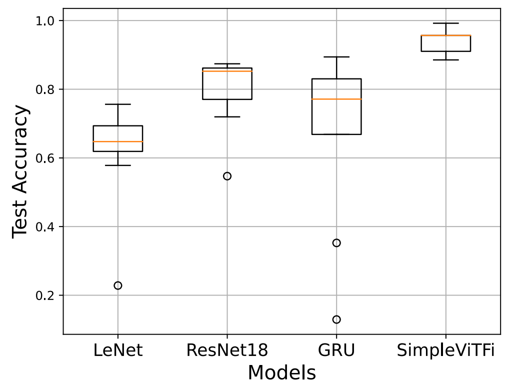


**Fig. 6** Test accuracy of Experiment 1 with amplitude values. TrainSet and TestSet consist of PI-1.

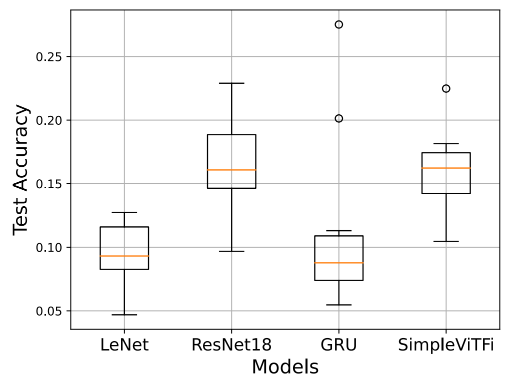


**Fig. 7** Test accuracy of Experiment 1 with phase values. TrainSet and TestSet consist of PI-1.

with the high median accuracy, underscores the robustness of SimpleViTFi, indicating that it consistently delivers high performance under various conditions.

In Experiment 2 shown in Fig. 8, similar trends are observed. The two experiments utilize CSI data generated from two distinct sets of devices. After training on their respective train sets, the model achieved commendable results on their test sets, with classification accuracies exceeding 95%. This indicates that SimpleViTFi is adept at adapting to both LOS and NLOS scenarios. Furthermore, the results from the NLOS condition in Experiment 2 even surpass those from the LOS condition in Experiment 1. This suggests that the

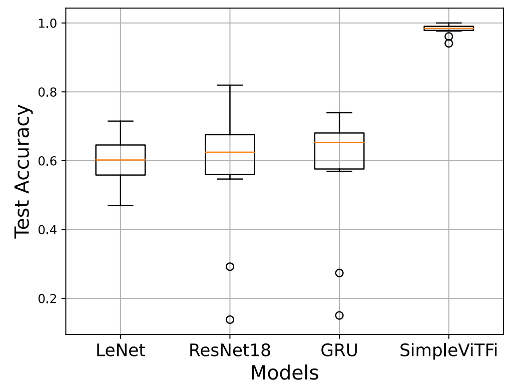


**Fig. 8** Test accuracy of Experiment 2 with amplitude values. TrainSet and TestSet consist of PI-4.

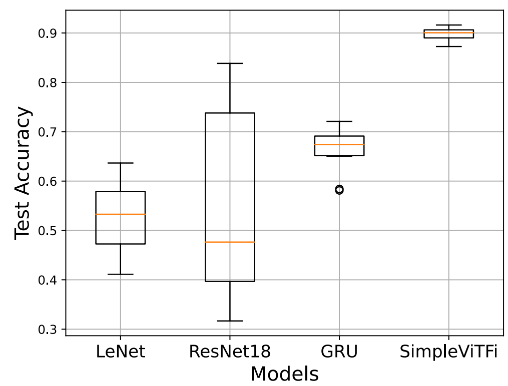


**Fig. 9** Test accuracy of Experiment 3 with amplitude values. TrainSet and TestSet consist of PI-1 & PI-3.

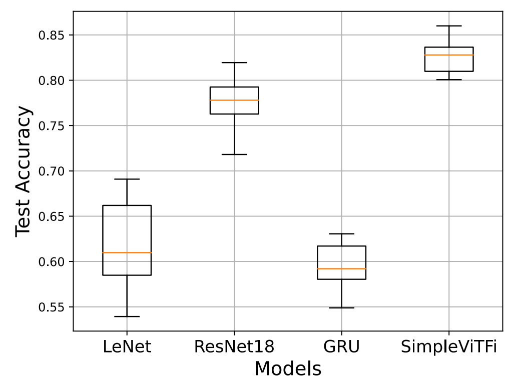


**Fig. 10** Test accuracy of Experiment 4 with amplitude values. TrainSet and TestSet consist of PI-1 & PI-2 & PI-3 & PI-4.

model might be benefiting from the distinct noise characteristics introduced by different devices.

We get similar results through Experiments 3 and 4. Through analyzing the box plots from Fig. 6 to Fig. 10, it is obvious that SimpleViTFi not only gets a high median accuracy but also demonstrates consistent performance, as indicated by the relatively small IQR, either on individual or mixed data sets generated by different devices or acquired by different monitors.

In conclusion, our experiments showcase the superior performance of the SimpleViTFi model in terms of both user identity recognition accuracy and inference time. By outperforming traditional methods, the SimpleViTFi model demonstrates its robustness and adaptability to various CSI data patterns.

### 4.5 Insights and Analysis

In the preceding subsections, we detail the architecture, Implementation, and evaluation of SimpleViTFi. Although the quantitative results indicate the model's efficacy, it is essential to dive deeper into the underlying mechanisms that contribute to its performance. In this subsection, we try to elucidate some of the key factors that are pivotal for the observed results.

(1) **Model Architecture**: SimpleViTFi employs a ViT-based architecture, which fundamentally differs from traditional convolutional (such as LeNet and ResNet18) and recurrent (such as GRU) neural networks. SimpleViTFi utilizes self-attention mechanisms to process input data. The self-attention mechanism is computationally expressed as:

$$\text{Attention}(\mathbf{Q}, \mathbf{K}, \mathbf{V}) = \text{softmax}\left(\frac{\mathbf{Q}\mathbf{K}^T}{\sqrt{d_k}}\right)\mathbf{V}, \quad (7)$$

where $\mathbf{Q}$, $\mathbf{K}$, and $\mathbf{V}$ are the query, key, and value matrices, respectively, and $d_k$ is the dimension of the key. The self-attention mechanism allows each element in the input sequence to focus on other parts, governed by the weight calculated in the softmax term.
The self-attention mechanism's ability to weigh and capture relationships between different parts of the input is particularly crucial for tasks involving WiFi CSI. In the context of CSI "images" classification, these relationships can be both spatial, as in different antenna pairs, and temporal, as in different time slots. Therefore, the self-attention mechanism, defined by the formula above, enables SimpleViTFi to capture these complex relationships efficiently.
On one hand, convolutional models struggle to capture the long or short-range dependencies inherent in time series data. On the other hand, while GRU can capture these temporal features, it computes in a time-step manner. In contrast, the self-attention mechanism stands out with its ability to address these challenges, offering both flexibility and parallelized computation. This makes SimpleViTFi highly effective and efficient in handling tasks that involve both spatial and sequential data.

(2) **Feature Representation Capability**: In traditional CNN architectures, the receptive field is generally localized, focusing primarily on capturing local features such as edges and textures. In contrast, SimpleViTFi leverages self-attention mechanisms to offer a dynamic receptive field, which allows the model to adaptively adjust its focus and capture features at various scales and complexities. The dynamic nature of its receptive field enables SimpleViTFi to integrate both local and global information more effectively, thereby providing an extra layer of flexibility and power in representing features.

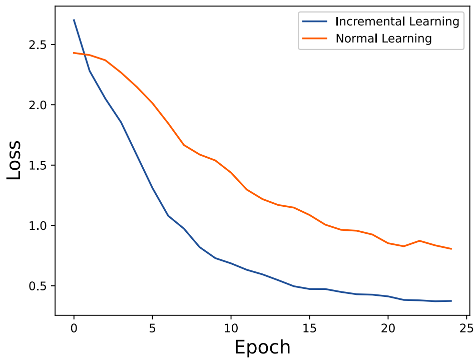

**Fig. 11** Loss curve of incremental SimpleViTFi and normal SimpleViTFi.

(3) **Training and Implementation Efficiency**: A significant advantage of SimpleViTFi lies in its efficiency. By utilizing only two transformer layers, the model inherently has fewer parameters as shown in Fig 5. This streamlined architecture not only expedites the training process but also ensures a swift inference time. Furthermore, the inherent parallel computation capability of the architecture further boosts the inference speed. As a result, SimpleViTFi boasts the shortest inference time among the four models, making it highly suitable for real-time applications.

(4) **Robustness to Noise and Deformation**: SimpleViTFi incorporates dropout layers in both the FeedForward and Attention modules. Dropout is a regularization technique that helps prevent overfitting, especially when the model might be exposed to sharp noise features in the data. Meanwhile, self-attention mechanism offers a more adaptive response to noise compared to other methods. Furthermore, the parallel processing capability ensures that SimpleViTFi remains resilient even when faced with temporal distortions in the data.

### 4.6 Incremental Learning

Based on the SimpleViTFi model trained in Experiment 3, we implement incremental learning [30]–[32] by training with a small amount of data from PI-4. As presented in Fig. 11, the loss curve of the incremental learning model converges faster than the normal one. Meanwhile, the accuracy of the incremental learning model is higher under the same training conditions.

## 5. Conclusion

In this paper, we introduce a novel Wi-Fi sensing method, SimpleViTFi, designed for Wi-Fi-based PI in cross-device sensing scenarios. To address the limitations of existing algorithms, we develop a lightweight neural network model

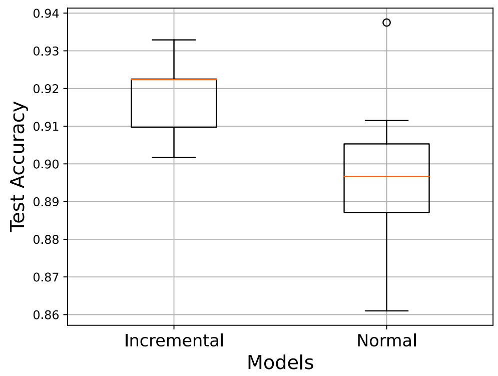


**Fig. 12** Test accuracy of incremental SimpleViTFi and normal SimpleViTFi.

based on ViT with learnable embedding. The original CSI data are generated by 2 pairs of Netgear and TP-Link Wi-Fi devices, which enable a single antenna to enforce the communication over a single spatial stream. The packets transmitted over-the-air by the Tx are monitored by 2 Asus routers equipped with 4 antennas and then form 4 folders containing both LOS and NLOS scenarios. Subsequently, we train the proposed SimpleViTFi under 4 experimental conditions, utilizing data generated by different devices or acquired by different monitors. Extensive experiments demonstrate that SimpleViTFi achieves state-of-the-art performance in test accuracy, inference time and model parameters compared to baseline methods (LeNet, ResNet18 and GRU). Finally, we experiment with incremental learning to obtain a new model at a low cost. Here, a SimpleViTFi model initially trained on one set of devices is subjected to incremental training on another set of devices with a small amount of additional data. The results show that better accuracy and faster convergence are gained compared to training directly with data from another set of devices.

In the future, we have several avenues of exploration to further enhance our research. Firstly, we plan to propose a new method of position encoding that is better adapted to the CSI-based classification. Our experiments have underscored the significant impact of this aspect on the results. Furthermore, we aim to delve deeper into the potential of utilizing various CSI parameters, such as phase values, Doppler shifts and AoA, to improve the model's performance. In addition, we intend to test our model on Wi-Fi devices based on OpenWrt and then conduct pilot tasks in substations within the State Grid of China. By pursuing these avenues, we hope to further refine our model and broaden its applicability, ultimately contributing to the advancement of Wi-Fi sensing technologies.

## Acknowledgments

This research was supported by the National Key R&D Program of China (No. 2020YFB2103300) and Science and Technology Project of State Grid Corporation of China (5108-202218280A-2-201-XG). The authors would like to thank the team behind [1], [14] for generously providing the dataset and assistance.

## References

[1] F. Meneghello, N. Dal Fabbro, D. Garlisi, I. Tinnirello, and M. Rossi, "A CSI dataset for wireless human sensing on 80 MHz Wi-Fi channels," IEEE Commun. Mag., vol.61, no.9, pp.146–152, 2023.

[2] "IEEE standard for information technology–telecommunications and information exchange between systems - local and metropolitan area networks–specific requirements - Part 11: Wireless LAN medium access control (MAC) and physical layer (PHY) specifications - redline," IEEE Std 802.11-2020 (Revision of IEEE Std 802.11-2016) - Redline, pp.1–7524, 2021.

[3] F. Restuccia, "IEEE 802.11bf: Toward ubiquitous Wi-Fi sensing," 2021.

[4] W. Jiang, H. Xue, C. Miao, S. Wang, S. Lin, C. Tian, S. Murali, H. Hu, Z. Sun, and L. Su, "Towards 3D human pose construction using WiFi," pp.295–308, Assoc Comp Machinery, 2020. 26th Annual International Conference on Mobile Computing and Networking (MobiCom), ELECTR NETWORK, Sept. 2020.

[5] D. Wu, Y. Zeng, F. Zhang, and D. Zhang, "WiFi CSI-based device-free sensing: From Fresnel zone model to csi-ratio model," CCF Trans. Pervasive Comp. Interact., vol.4, no.1, pp.88–102, March 2022.

[6] K. Niu, X. Wang, F. Zhang, R. Zheng, Z. Yao, and D. Zhang, "Rethinking Doppler effect for accurate velocity estimation with commodity WiFi devices," IEEE J. Sel. Areas Commun., vol.40, no.7, pp.2164–2178, July 2022.

[7] J. Yang, X. Chen, H. Zou, D. Wang, and L. Xie, "AutoFi: Towards automatic Wi-Fi human sensing via geometric self-supervised learning," IEEE Internet Things J., vol.10, no.8, pp.7416–7425, 2023.

[8] J. Yang, X. Chen, H. Zou, D. Wang, Q. Xu, and L. Xie, "EfficientFi: Toward large-scale lightweight WiFi sensing via CSI compression," IEEE Internet Things J., vol.9, no.15, pp.13086–13095, 2022.

[9] Y. Yang, K. McLaughlin, L. Gao, S. Sezer, Y. Yuan, and Y. Gong, "Intrusion detection system for IEC 61850 based smart substations," 2016 IEEE Power and Energy Society General Meeting (PESGM), pp.1–5, 2016.

[10] S. Qiao, Q. Zheng, W. Li, S. Yang, and H. Zhang, "Intrusion detection of intelligent substation video surveillance based on average background interframe difference method," 2023 IEEE 2nd International Conference on Electrical Engineering, Big Data and Algorithms (EEBDA), pp.1023–1026, 2023.

[11] P.M. Mammen, C. Zakaria, T. Molom-Ochir, A. Trivedi, P. Shenoy, and R. Balan, "WiSleep: Inferring sleep duration at scale using passive WiFi sensing," 2022.

[12] F. Wang, Y. Song, J. Zhang, J. Han, and D. Huang, "Temporal Unet: Sample level human action recognition using WiFi," 2019.

[13] G. Yin, J. Zhang, G. Shen, and Y. Chen, "FewSense, towards a scalable and cross-domain Wi-Fi sensing system using few-shot learning," IEEE Trans. Mobile Comput., vol.23, no.1, pp.453–468, 2024.

[14] F. Meneghello, D. Garlisi, N.D. Fabbro, I. Tinnirello, and M. Rossi, "SHARP: Environment and person independent activity recognition with commodity IEEE 802.11 access points," IEEE Trans. Mobile Comput., vol.22, no.10, pp.6160–6175, 2023.

[15] S.M. Hernandez and E. Bulut, "WiFederated: Scalable WiFi sensing using edge-based federated learning," IEEE Internet Things J., vol.9, no.14, pp.12628–12640, 2022.

[16] Y. Liu, S. Li, J. Yu, A. Dong, L. Zhang, C. Zhang, and Y. Cao, "WiFi sensing for drastic activity recognition with CNN-BiLSTM architecture," 2022 IEEE International Conference on Systems, Man, and Cybernetics (SMC), IEEE, 2022.

[17] T. Xin, B. Guo, Z. Wang, M. Li, Z. Yu, and X. Zhou, "FreeSense: Indoor human identification with Wi-Fi signals," 2016 IEEE Global Communications Conference (GLOBECOM), pp.1–7, 2016.

[18] C. Lin, P. Wang, C. Ji, M.S. Obaidat, L. Wang, G. Wu, and Q. Zhang, "A contactless authentication system based on WiFi CSI," ACM

Trans. Sensors Netw., vol.19, no.2, pp.1–20, May 2023.

[19] W. Li, M.J. Bocus, C. Tang, S. Vishwakarma, R.J. Piechocki, K. Woodbridge, and K. Chetty, "A taxonomy of WiFi sensing: CSI vs passive WiFi radar," 2020 IEEE Globecom Workshops (GC Wkshps), pp.1–6, 2020.

[20] M.A. Khalighi, S. Long, S. Bourennane, and Z. Ghassemlooy, "PAM- and CAP-based transmission schemes for visible-light communications," IEEE Access, vol.5, pp.27002–27013, 2017.

[21] A. Dosovitskiy, L. Beyer, A. Kolesnikov, D. Weissenborn, X. Zhai, T. Unterthiner, M. Dehghani, M. Minderer, G. Heigold, S. Gelly, J. Uszkoreit, and N. Houlsby, "An image is worth 16x16 words: Transformers for image recognition at scale," 2021.

[22] Y. Xu, H. Wei, M. Lin, Y. Deng, K. Sheng, M. Zhang, F. Tang, W. Dong, F. Huang, and C. Xu, "Transformers in computational visual media: A survey," Comp. Visual Media, vol.8, no.1, pp.33–62, March 2022.

[23] O. Moutik, H. Sekkat, S. Tigani, A. Chehri, R. Saadane, T.A. Tchakoucht, and A. Paul, "Convolutional neural networks or vision transformers: Who will win the race for action recognitions in visual data?," Sensors, vol.23, no.2, 734, Jan. 2023.

[24] Y. Zhao, J. Li, X. Chen, and Y. Tian, "Part-guided relational transformers for fine-grained visual recognition," IEEE Trans. Image Process., vol.30, pp.9470–9481, 2021.

[25] A. Vaswani, N. Shazeer, N. Parmar, J. Uszkoreit, L. Jones, A.N. Gomez, L. Kaiser, and I. Polosukhin, "Attention is all you need," arXiv, arXiv:1706.03762, 2017.

[26] F. Gringoli, M. Schulz, J. Link, and M. Hollick, "Free your CSI: A channel state information extraction platform for modern Wi-Fi chipsets," WiNTECH'19, New York, NY, USA, pp.21–28, Association for Computing Machinery, 2019.

[27] W.C. Yeh, Y.P. Lin, Y.C. Liang, and C.M. Lai, "Convolution neural network hyperparameter optimization using simplified swarm optimization," 2021.

[28] M. Kashif, "Urdu handwritten text recognition using ResNet18," 2021.

[29] X. Li, C. Wang, X. Huang, and Y. Nie, "A GRU-based mixture density network for data-driven dynamic stochastic programming," 2020.

[30] Z. Wu, C. Baek, C. You, and Y. Ma, "Incremental learning via rate reduction," IEEE Computer Society Conference on Computer Vision and Pattern Recognition, 2021.

[31] S. Mittal, S. Galesso, and T. Brox, "Essentials for class incremental learning," 2021.

[32] G.M. van de Ven, T. Tuytelaars, and A.S. Tolias, "Three types of incremental learning," Nat. Mach. Intell., vol.4, pp.1185–1197, 2022.

**Jichen Bian** received the B.S. degree in Electronic Information Science and Technology from Zhengzhou University, Zhengzhou, China, in 2019. He is currently pursuing the Ph.D. degree in Commnuication and Information System with Shanghai Institute of Microsystem and Information Technology, CAS. His research interests include Wi-Fi-based integrated sensing and communications, heterogeneous network resource allocation technology, and wireless sensor networks.

**Min Zheng** received the Ph.D. degree in Commnuication and Information System from Beijing University of Posts and Telecommunications, Beijing, China, in 2006. He is currently a Professor at the Laboratory of Broadband Wireless Technology, Shanghai Institute of Microsystem and Information Technology, CAS. His research interests include Automatic configuration technology for self-organizing networks and emergency applications of broadband wireless communication systems.

**Hong Liu** received the B.S. and Ph.D. degrees in 2003 and 2011, respectively, from the School of Information Science and Technology, Peking University, Beijing, China. He is currently a Professor at the Laboratory of Broadband Wireless Technology, Shanghai Institute of Microsystem and Information Technology, CAS. His research interests include broadband self-assembling networks, 4G/5G communications and communications in complex electromagnetic/terrain environments.

**Jiahui Mao** received the B.S. degree in Electronic Information Engineering from Zhejiang University of Technology, Hangzhou, China, in 2020. He is currently pursuing the Ph.D. degree in Commnuication and Information System with Shanghai Institute of Microsystem and Information Technology, CAS. His research interests include resource management for wireless networks, mobile edge computing, and wireless sensor networks.

**Hui Li** received the Ph.D. degree in 2012 from the School of Communications and Information Engineering, Tongji University, Shanghai, China. She is currently a Professor at the Laboratory of Broadband Wireless Technology, Shanghai Institute of Microsystem and Information Technology, CAS. Her research interests include wireless ad-hoc network, artificial intelligence and communication.

**Chong Tan** received the M.S. and Ph.D. degrees in 2009 and 2013, respectively, from the School of Communications and Information Engineering, Shanghai University, Shanghai, China. She is currently a Professor at the Laboratory of Broadband Wireless Technology, Shanghai Institute of Microsystem and Information Technology, CAS. Her research interests include Internet of Things, sensing and positioning, edge computing, etc.